Geosystems and Geoenvironment 1 (2022) 100040

Contents lists available at ScienceDirect

Geosystems and Geoenvironment

journal homepage: www.elsevier.com/locate/geogeo

Petrogenesis of Bonai volcanic rocks from Singhbhum Craton (Eastern India): Geophysical and geodynamic implications for pervasive plume-lithospheric interaction

S.K. Dwivedi[a], O.P. Pandey[b,*], Priyanka Tripathi[a], S.H. Jafri[b], D. Srinivasa Sarma[b], A. Narsing Rao[c], Prachiti Kanakdande[b], G. Parthasarathy[d]

[a] Geological Survey of India, Bandlaguda, Hyderabad 500068, India
[b] CSIR-National Geophysical Research Institute, Uppal Road, Hyderabad 500007, India
[c] Geology Department, Osmania University, Hyderabad 500007, India
[d] National Institute of Advanced Studies, School of Natural Science and Engineering, Indian Institute of Science Campus, Bangalore 560012, India

A R T I C L E I N F O

Article history:
Received 12 December 2021
Revised 5 February 2022
Accepted 12 February 2022

Keywords:
Geochemistry
Bonai volcanic complex
Singhbhum Craton
Mantle potential temperature
Mantle plume-lithospheric interaction
Geophysical and geodynamic implications

A B S T R A C T

Singhbhum Craton of the Indian Shield is one of the oldest Eoarchean segments on the Earth, which contains several well-preserved Mesoarchean-Paleoproterozoic volcanic suites. In this study, we investigate petrogenesis of the Bonai suite of volcanic rocks located in the western part of the craton on the basis of detailed geological, geochemical and geophysical data, which provide a new understanding of its regional geodynamic evolution. These volcanics are generally fine to medium-grained, exhibit porphyritic texture and contain plagioclase and pyroxene as primary minerals and amphiboles, epidote, sericite and chlorite as secondary minerals. The accessory phases are mainly zircon, ilmenite, pyrite and chalcopyrite. They can be petrographically and geochemically classified as basalt and basaltic andesite of tholeiitic nature. They are characterized by moderate to high contents of SiO_2 (49.35–57.81 wt%), MgO (7.14–11.39 wt%), Al_2O_3 (10.21–14.68 wt%), CaO (5.14–11.15 wt%), TiO_2 (0.48–2.03 wt%), Cr (32–483 ppm) and Ni (34–175 ppm). Their HFSE/REE ratios and REE patterns indicate their derivation from a relatively low melting of a similar mantle source within the spinel lherzolite stability field. They are formed as a result of decompressive melting of the mantle plume near the crust-mantle boundary, which underwent fractional crystallization and crustal contamination. The plume had an initial mantle potential temperature between 1300 °C and 1700 °C with corresponding pressure of 0.5 to 3.5 GPa. In Nb/Y-Zr/Y plot, almost all the samples fall in the field of oceanic plateau basalt with mantle plume affinity. This region is underplated by about 14 km thick magmatic rocks above the Moho, over which gravity field and regional elevation are consistently high and the lithosphere is extremely thin. These characteristics corroborate well with the mantle plume signatures. Subduction related geochemical signatures appear absent.

1. Introduction

Indian Shield is considered as a mosaic of five Archean cratonic segments, which are welded together by active mobile belts, Gondwana rift valleys, suture zones and mega lineaments that remained active since Mesoproterozoic to present (Rogers and Callahan, 1987). Out of these cratonic segments, Singhbhum Craton located in the eastern part of the Indian Shield is considered one of the oldest (Chaudhuri et al., 2018; Olierook et al., 2019; Sreenivas et al., 2019; Mukhopadhyay and Matin, 2020), and most deformed/decratonized Archean segments on the surface of the Earth (Pandey, 2020; Vasanthi et al., 2021), in a way similar to the eastern part of the North China Craton (Li and Santosh, 2014; Xia et al., 2017; Wu et al., 2019; Vasanthi and Santosh, 2021). Geophysically, this craton does not possess characteristics of a typical stable shield and differs considerably from other stable areas of the Earth (Negi et al., 1986; Polat and Anderson, 1995; Pandey and Agrawal, 1999; Artemieva and Mooney, 2001; Kumar et al., 2013; Pandey, 2020; Vasanthi et al., 2021). It is conspicuously characterized by positive gravity field (GSI-NGRI, 2006; Tiwari et al., 2013;

* Corresponding author.
E-mail address: om_pandey@rediffmail.com (O.P. Pandey).

https://doi.org/10.1016/j.geogeo.2022.100040

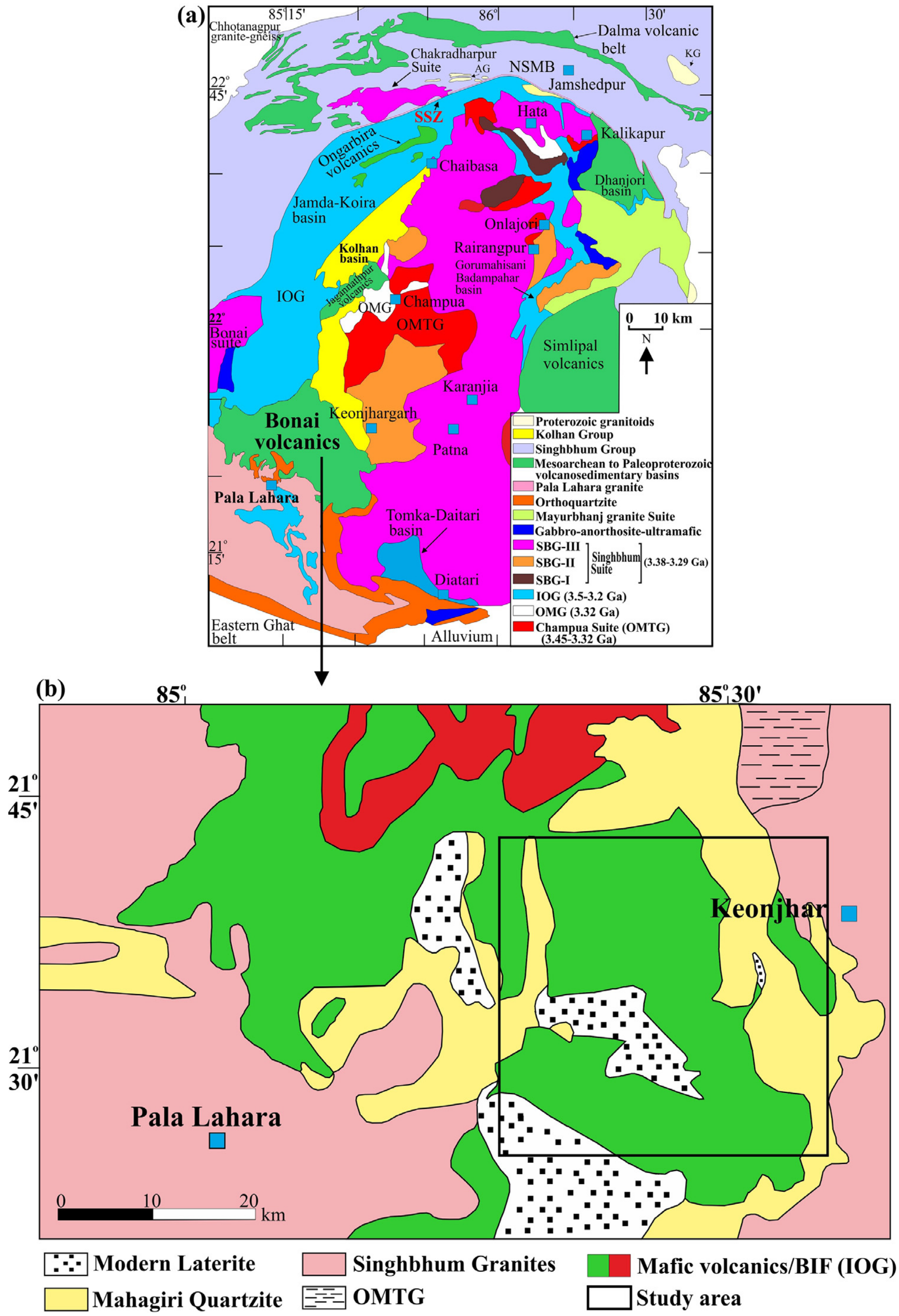

Fig. 1. (a) Geological map of the Singhbhum craton, eastern India (modified after Dey et al., 2017, 2019). OMTG: Older Metamorphic Tonalitic Gneiss; OMG: Older Metamorphic Group; IOG: Iron Ore Group; SBG: Singhbhum granitic suites; NSMB: North Singhbhum Mobile Belt; SSZ: Singhbhum Shear Zone. Age data of different suites are based on the studies of Misra et al. (1999), Saha et al. (2012), Nelson et al. (2014), Upadhyay et al. (2014, 2019), Dey et al. (2017, 2019), Dey and Moyen (2020). (b) Geology of south-western IOG (After Sreenivas et al., 2019). Black rectangle shows the area of present study.

Vasanthi et al., 2021) and an unusually thin (65–95 km) and warm lithosphere due to large scale destruction of the cratonic keel (Pandey and Agrawal, 1999; Shalivahan et al., 2014; Mandal, 2017; Pandey, 2020). The Crozet hot spot has passed through the center of this craton (Curray and Munasinghe, 1991).

This craton which covers an area of around 50,000 km^2, is largely made up of the Paleoarchean granitoid core, surrounded by Paleoarchean to Paleoproterozoic volcano-sedimentary/greenstone belts. It conspicuously contains several mafic-ultramafic occurrences as well (Banerjee, 1982; Mukhopadhyay and Dutta, 1983; Acharyya, 1993; Basu et al., 1997; Sengupta et al., 1997; Bose, 2009; Acharyya et al., 2010a, b). The earliest phase of magmatic activity is marked by the occurrence of mafic enclaves within the Paleoarchean Older Metamorphic Group of rocks. In comparison, the next phase of mafic magmatism, which was more prolific, took place during the Mesoarchean-Paleoproterozoic.

Fig. 2. Field photographs showing exposures of Bonai volcanics in Pala Lahara-Keonjhar area. (a) Aerial view of studied volcanics exposed in a nala section, and (b) along road side, southwest of Keonjhar. These volcanics are fine to medium grained, massive and devoid of secondary veins like quartz and carbonates.

This phase is represented by Ongarbira, Dalma, Dhanjori, Jagannathpur, Simplipal, and Bonai (also known as Malangtoli) volcanic suites and mafic dykes (Fig. 1) emplacements (Newer dolerites) which occupied a considerable part of this craton (Saha, 1994; Mukhopadhyay, 2001; Roy et al., 2005; Mondal et al., 2006; Manikyamba et al., 2015; Anil Kumar et al., 2017; Ravi Shankar et al., 2018; Arif et al., 2021; Fig. 1). The Bonai volcanics, which is the area of the present investigation, are exposed as thick formations of massive undeformed lavas in its western part. They are associated with the Banded Iron ore Formations in Iron Ore Group (IOG) (Banerjee, 1982; Mahadevan, 2002; Ray et al., 2006; Singh et al., 2017) and are exposed along the Keonjhargarh-Pala Lahara Road and nearby regions (Fig. 1). Petrologically, these lavas are more evolved than other BIF lavas (Saha, 1994; Mahadevan, 2002) and relatively depleted in magnesian. They have been considered equivalent to Jagannathpur volcanics (Saha, 1994) in the north. The minimum crystallization age calculated by the Pb-Pb zircon methods for the acid volcanics, located west of the studied volcanics, suggest that the Bonai volcanics could be older than 2.8 Ga (Bandyopadhyay et al., 2001). Systematic geochemical studies over these volcanics are limited to a few areas (Ray et al., 2006; Banerjee et al., 2016; Singh et al., 2017). The present study deals with petrographical, geochemical and geophysical investigations over this volcanic suite exposed in a vast area between Keonjhargarh and Pala Lahara Road sections and their surrounding areas (Fig. 1). The present study points out the role of mantle plume induced crust-mantle interaction for their genesis and thus has a relevance to our understanding of magmatism associated with deformed Precambrian terrains.

2. Geological setting

Singhbhum Craton located in the eastern part of the Indian Peninsular Shield represents Eoarchean crust characterized by complex geological settings (Saha, 1994; Misra, 2006; Nelson et al., 2014; Chaudhuri et al., 2018; Pandey et al., 2019; Chaudhuri, 2020; Olierook et al., 2019; Sreenivas et al., 2019). As mentioned before, it is associated with unusual geophysical signatures (Pandey, 2020 and references therein). It is bounded by the Sukinda thrust zone in the south, Eastern Ghats Belt to the southeast, the Bastar Craton to the southwest, and the North Singhbhum Mobile Belt and Proterozoic Chotanagpur gneissic complex in the north (Misra and Johnson, 2005; Mondal et al., 2006; Roy and Bhattacharya, 2012).

This craton primarily consists of Paleo-to Mesoarchean granitoid complex exposed over vast tract (Fig. 1) in which Paleoarchean Older Metamorphic Tonalite Gneiss complex (OMTG), also known as Champua suite (2.45–3.32Ga), is considered the oldest (Saha, 1994; Upadhyay et al., 2014; Nelson et al., 2014; Dey et al., 2017; Pandey et al., 2019; Chaudhury, 2020; Dey and Moyen, 2020). Recently, xenocrystic zircons of 4.24–4.03 Ga have also been reported from the TTG suites of this complex (Chaudhuri et al., 2018). Older Metamorphic Group (OMG) is another primary supracrustal assemblage which is made up of amphibolite facies rocks, metapelites, calc-silicate rocks and quartzites (Saha, 1994; Hofmann and Mazumdar, 2015) and exposed on the western side of the OMTG (Saha et al., 2012; Mazumder et al., 2015; Pandey et al., 2019; Upadhyay et al., 2019). OMTG rocks form the basement of the OMG rocks. Both the units (OMTG and OMG) are in direct contact with the 3.38–3.29 Ga Singhbhum granitoid suite, also popularly known as Singhbhum granites (Nelson et al., 2014; Upadhyay et al., 2014; Dey et al., 2017, 2019; Pandey et al., 2019), which are made up of granite and TTG rocks, spread over an area of almost 8000 km^2 in the central part. This suite is encircled by Iron Ore Group (IOG) supracrustal belts, consisting of greenschist to amphibolite facies metasedimentary rocks, inter-layered with mafic/ultramafic and minor felsic volcanics (Upadhyay et al., 2019; Dey and Moyen, 2020). They are distributed over Gorumahisani-Badampahar, Jamda-Koira and Daitari-Pala Lahara basins (Saha, 1994; Mukhopadhyay et al., 2012). This craton is also characterized by several A-type granitoids in its NE and SW parts, like Mayurbhanj and Pala Lahara suites, emplaced around 3.1–2.8 Ga, which were subsequently followed by a number of volcanic suites and episodic mafic dyke swarms activity (Newer dolerites) between 2.80 Ga and 1.76 Ga (Saha, 1994; Mukhopadhyay, 2001; Roy et al., 2005; Mondal et al., 2006; Anil Kumar et al., 2017; Ravi Shankar et al., 2018). Many discrete gabbro-anorthosite complex of the pre-Singhbhum granitic emplacement period are also present in the eastern and southern part of the craton (Saha, 1994; Roy and Bhattacharya, 2012).

The Bonai mafic volcanics, which is one of the prominent volcanic terrains of this craton, is relatively felsic than the other volcanic suites. They can be seen exposed between Keonjhargarh and Pala Lahara (Fig. 1) and their surrounding areas, covering around 800 km^2 (Saha, 1994; Ray et al., 2006). These lavas overlie an unconformity in southern part and consists of quartz-sandstone pebble beds designated as Mankharchua Group (Sarkar et al., 1986). These volcanic rocks are overlain by the Kolhan Group of sandstones and shales at the eastern side. To the west of Koenjhar, the Bonai volcanic rocks have a faulted contact with the Banded Iron Formations of IOG (Ramakrishnan and Vaidyanadhan, 2008). In some areas like Kanjipani area of Malangtoli, mafic lavas are associated with quartzites, ironstones, conglomerates and talc schist (Banerjee et al., 2016) with laterite as the cap rock. In general, the Bonai volcanic rocks are massive and predominantly mafic, with sporadic occurrences of poorly preserved pillow structures that

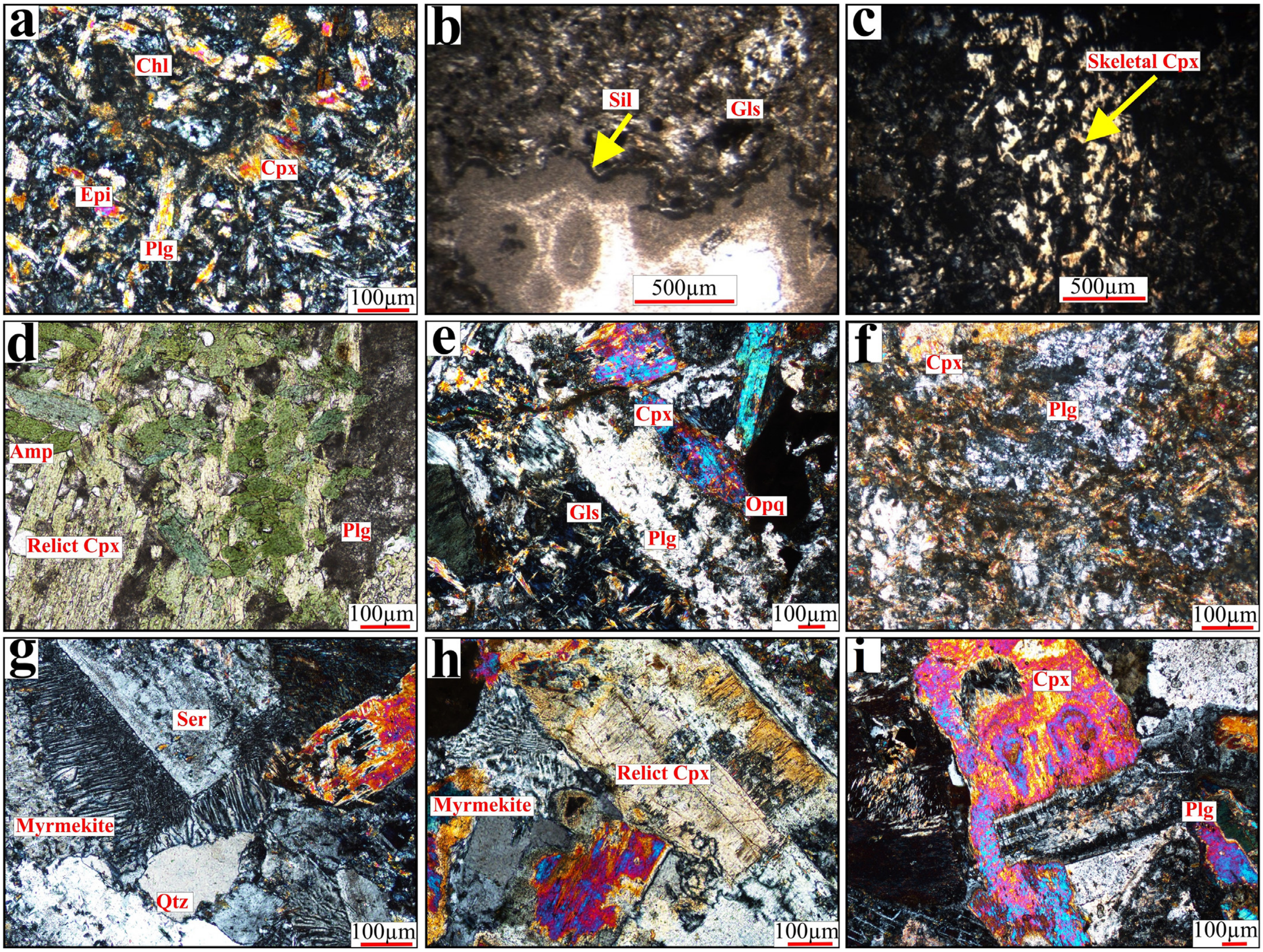

Fig. 3. Photomicrographs of Bonai volcanic rocks showing presence of plagioclase and pyroxene as primary minerals and epidote and chlorite as secondary minerals. They exhibit overall porphyritic texture with the groundmass composition marked by plagioclase and clinopyroxene (a, d, e, h and i). Some of the thin sections have shown presence of silica in voids (OP-75/5; b). The presence of saussuritized plagioclase (OP-84/05; i) and secondary amphiboles (uralitization) (d) indicate that these rocks are affected by hydrothermal alteration. The presence of relict and skeletal pyroxene (OP-87/05; c) also suggests hydrothermal alteration. Few samples exhibit myrmekite texture (g, h). Ophitic texture can be seen in Fig. 3i. Plg: Plagioclase; Cpx: Clino-pyroxene; Epi: Epidote; Chl: Chlorite; Sil: Silica; Gls: Glass; Amp: Amphiboles; Opq: Opaques; Ser: Sericite; Qtz: Quartz.

are sheared, deformed and chloritized, penetrated occasionally by quartz and carbonate veins.

3. Sampling and analytical techniques

Samples that are least altered, homogeneous and devoid of secondary quartz and carbonates are collected from the freshest part of the outcrops (Fig. 2a, b). Thin sections of the selected samples were prepared and studied at CSIR-NGRI, Hyderabad, and Southern region laboratory of Geological Survey of India, Hyderabad. After thorough petrographic observations, 21 samples were selected for the analysis of major and trace (including REE), which was also carried out at CSIR-National Geophysical Research Institute, Hyderabad. Major oxides were analyzed using Philips Magix PRO model PW2440 wavelength dispersive X-ray fluorescence spectrophotometer (XRF), which is coupled with an automatic sample changer PW-2540. The instrument is microprocessor-controlled for maximum flexibility. Oxides are measured with a precision of 1% and 2%. The precision and accuracy of XRF data measured by this machine have earlier been reported in detail by Krishna et al. (2007). Standard reference materials used are BHVO-1 and BCR-1. Similarly, the trace elements (including Rare Earth Elements) were determined by ICP-MS (ELAN DRC II). Analytical data presented here have a reproducibility of measurements better than + 5% RSD (Relative Standard Deviation) for all the trace elements. The precision and accuracy of the measured data from this instrument are discussed in detail elsewhere by Balaram and Rao (2003). Standard reference materials used in this study are JB-2, BHVO-1 and BCR-1. Measured values of major oxides and trace elements are presented in Table 1 and Table 2. Major oxides values are on an anhydrous 100% adjusted basis.

To further confirm the altered mineral phases and opaque minerals, Scanning Electron Microscope (SEM) study was carried out. The BSE images provided the minerals surface morphology and independent confirmation of mineral compositions. This study used Hitachi, S-3400 N Scanning Electron Microscope (SEM) coupled with energy dispersive spectrometer (EDS) at CSIR-NGRI, Hyderabad. Spot analysis of different minerals and backscattered electron (BSE) imaging were carried out to understand the compositions and variations of the various ore mineral phases. 15 kV accelerating voltage was used to get high-resolution images from the samples. Other parameters like magnification, working distance

Table 1
Whole rock major oxides (wt%) and CIPW norm data of basalt (B) and basaltic andesite (BA) from Bonai volcanic region, Singhbhum Craton. Major oxides values are on an anhydrous basis.

Sample **Rock-type**	**OP 87/05** **B**	**OP 74/05** **B**	**OP 83/05** **B**	**OP 81/05** **B**	**OP 91/05** **B**	**OP 75/05** **B**	**OP 79/05** **B**	**OP 76/05** **B**	**OP 84/05** **B**	**OP 86/05** **B**	**OP 92/05** **BA**	**OP 72/05** **BA**	**OP 77/05** **BA**	**OP 89/05** **BA**	**OP 90/05** **BA**	**OP 88/05** **BA**	**OP 80/05** **BA**	**OP 78/05** **BA**	**OP 85/05** **BA**	**OP 82/05** **BA**	**OP 73/05** **BA**
SiO_2	49.35	49.6	50	50.37	51	51.6	51.97	52	51.6	52	52.2	52.8	53.6	53.97	54.15	54.79	55.3	55.57	55.6	55.6	57.81
TiO_2	1.49	1.66	1.81	2.03	0.73	1.18	0.72	1.05	1.02	1.55	1.41	0.87	0.64	0.71	0.74	0.69	0.75	0.62	0.69	0.67	0.48
Al_2O_3	13.31	12	12.4	11.25	12	13.36	13.03	12.8	12.6	12.2	11.2	12.8	12.9	12.41	10.29	13.47	10.5	10.21	13.7	11.7	14.68
Fe_2O_3	13.89	15.8	13.3	14.3	12.4	11.03	13.07	13.9	13.9	12.5	12.7	11.5	11	11.98	10.93	10.84	11.6	9.45	9.68	10.8	2.2
MnO	0.17	0.19	0.21	0.2	0.19	0.14	0.18	0.17	0.17	0.18	0.17	0.16	0.15	0.15	0.16	0.16	0.16	0.13	0.16	0.15	0.09
MgO	8.73	8.78	7.54	7.79	9.34	11.39	9.76	7.14	7.74	7.91	8.15	8.02	9.71	9.57	10.23	10.14	10	8.84	9.63	9.27	9.78
CaO	9.82	7.86	9.92	9.44	10.4	7.42	6.55	8.37	8.44	7.57	9.02	8.75	7.48	5.98	9.02	5.14	7.29	11.15	5.43	6.83	6.63
Na_2O	1.65	2.83	2.35	2.3	2.37	1.81	1.85	3.09	2.8	3.01	2.2	3.1	1.38	2.18	1.65	2.26	2.04	1.62	2.04	2.46	0.45
K_2O	0.5	0.91	0.53	0.74	0.41	0.8	1.53	1.29	1.05	1.14	1.19	1.04	1.61	1	1.27	1.1	0.76	0.42	1.06	1.06	6.27
P_2O_5	0.23	0.13	0.25	0.37	0.08	0.24	0.07	0.26	0.27	0.26	0.23	0.2	0.08	0.07	0.08	0.08	0.08	0.06	0.08	0.08	0.09
Total	99.14	99.9	98.4	98.79	99	98.97	98.73	100	99.5	98.4	98.5	99.3	98.6	98.02	98.52	98.67	98.4	98.07	98	98.6	98.48
Na_2O+K_2O	*2.15*	*3.74*	*2.88*	*3.04*	*2.78*	*2.61*	*3.38*	*4.38*	*3.85*	*4.15*	*3.39*	*4.14*	*2.99*	*3.18*	*2.92*	*3.36*	*2.8*	*2.04*	*3.1*	*3.52*	*6.72*
CIPW norm																					
Quartz	8.70	4.67	8.07	9.03	6.20	7.81	8.98	6.11	7.00	7.05	9.62	5.87	11.81	12.33	11.24	11.88	14.21	15.32	14.17	12.37	5.42
Orthoclase	2.95	5.38	3.13	4.37	2.42	4.73	9.04	7.62	6.21	6.74	7.03	6.15	9.51	5.91	7.51	6.50	4.49	2.48	6.26	6.26	37.05
Albite	13.96	23.95	19.88	19.46	20.05	15.32	15.65	26.15	23.69	25.47	18.62	26.23	11.68	18.45	13.96	19.12	17.26	13.71	17.26	20.82	3.81
Anorthite	27.43	17.46	21.83	18.19	21.00	25.97	22.73	17.19	18.76	16.49	17.25	18.05	24.25	21.12	16.92	23.36	17.17	19.35	25.09	17.70	19.52
Diopside	11.90	11.96	15.81	15.56	22.05	4.46	5.85	15.32	14.40	11.44	16.97	16.89	8.34	4.84	19.78	–	12.86	26.46	–	10.86	8.94
Hypersthene	16.24	16.34	11.47	12.21	13.06	26.31	21.60	10.70	12.62	14.41	12.45	12.16	20.33	21.60	16.33	25.26	18.98	9.78	23.99	18.07	20.22
Ilmenite	0.36	0.41	0.45	0.43	0.41	0.30	0.38	0.36	0.36	0.38	0.36	0.34	0.32	0.32	0.34	0.34	0.34	0.28	0.34	0.32	0.19
Apatite	0.53	0.30	0.58	0.86	0.19	0.56	0.16	0.60	0.63	0.60	0.53	0.46	0.19	0.16	0.19	0.19	0.19	0.14	0.19	0.19	0.21
Hematite	13.89	15.82	13.34	14.30	12.42	11.03	13.07	13.85	13.87	12.49	12.71	11.49	11.00	11.98	10.93	10.84	11.57	9.45	9.68	10.78	2.20
Titanite	3.19	3.55	3.86	4.43	1.27	2.51	1.27	2.11	2.03	3.31	2.99	1.69	1.16	1.33	1.37	1.14	1.40	1.16	0.93	1.23	0.93
S.I.	37.97	28.67	37.95	35.25	40.63	35.23	28.48	31.47	32.26	31.27	35.91	35.89	34.84	28.29	39.44	26.58	33.66	49.25	29.82	32.32	42.64
D.I.	25.62	33.99	31.09	32.86	28.67	27.85	33.67	39.88	36.90	39.26	35.27	38.25	33.00	36.68	32.70	37.50	35.96	31.51	37.69	39.45	46.29
AI	45	48	40	42	43	57	57	42	44	46	45	43	56	56	52	60	54	42	59	53	69
Mg#	55.5	52.4	52.8	51.9	59.8	67.2	59.7	50.5	52.5	55.6	55.9	58	63.6	61.3	65	65	63.2	64.9	66.3	63	89.8

DI = Differentiation Index. SI = Solidification Index. $Mg^{\#} = 100\ Mg^{2+}/(Mg^{2+} + Fe^{2+})$. Rock-types are classified according to total alkalis versus silica diagram (Le Bas et al., 1986; Le Bas, 1989, 2000. CIPW norms are on an anhydrous 100% adjusted basis using Fe_2O_3/FeO ratio after Middlemost (1989) and following the SINCLAS computer program (Verma et al., 2002). AI = Alteration Index: $100(K_2O + MgO)/(K_2O + MgO + Na_2O + CaO)$ (Ishikawa et al., 1976; Large, 2001).

Table 2
Trace elements and REEs data of basalt (B) and basaltic andesite (BA) from Bonai volcanic region, Singhbhum Craton.

Sample	OP 87/05	OP 74/05	OP 83/05	OP 81/05	OP 91/05	OP 75/05	OP 79/05	OP 76/05	OP 84/05	OP 86/05	OP 92/05	OP 72/05	OP 77/05	OP 89/05	OP 90/05	OP 88/05	OP 80/05	OP 78/05	OP 85/05	OP 82/05	OP 73/05
Rock-type	**B**	**B**	**B**	**B**	**B**	**B**	**B**	**B**	**B**	**B**	**BA**	**BA**	**BA**	**BA**	**BA**	**BA**	**BA**	**BA**	**BA**	**BA**	**BA**
Sc	28	38	33	29	38	28	29	20	19	34	27	19	29	28	33	28	29	28	27	27	4
V	179	337	285	296	201	185	209	203	202	279	202	175	152	164	184	160	174	149	160	153	27
Cr	157	178	136	95	116	310	216	135	167	122	32	329	359	306	483	212	324	201	199	272	131
Co	46	92	52	89	45	44	46	98	45	51	38	98	47	86	53	92	119	40	77	123	13
Ni	98	99	71	74	73	114	93	79	99	67	54	75	112	117	175	118	130	83	115	120	34
Cu	135	194	161	146	97	101	66	142	135	150	104	123	76	97	86	89	92	71	87	78	41
Zn	86	96	117	96	59	61	64	71	73	94	78	71	64	59	55	76	58	46	78	60	34
Ga	18	17	17	18	13	14	19	18	17	17	16	16	13	13	14	15	13	16	15	14	6
Rb	10	16	16	13	9	33	47	27	21	17	33	23	49	32	47	47	24	11	47	41	56
Sr	190	109	160	135	116	108	87	204	209	162	231	210	121	119	214	185	120	173	183	212	22
Y	28	27	34	44	17	28	22	21	21	33	42	16	30	21	22	21	22	19	21	18	11
Zr	121	81	123	182	29	172	91	135	125	120	239	96	112	105	106	99	106	81	101	98	64
Nb	7	5	6	12	2	11	5	8	8	6	17	6	6	6	6	5	6	5	5	5	5
Cs	0	0	4	0	0	0	0	1	0	4	0	1	0	0	0	0	0	0	0	0	1
Ba	81	174	121	83	18	70	110	178	195	86	152	120	168	143	154	175	88	32	175	128	327
La	10.84	6.19	8.66	18.31	3.00	18.54	14.02	16.36	16.62	8.46	30.72	13.25	16.50	16.16	15.73	16.26	15.91	13.17	16.70	16.93	16.33
Ce	24.62	15.99	21.56	42.20	7.29	39.27	29.60	33.79	34.14	20.80	63.69	27.71	33.38	33.18	32.68	33.07	32.82	27.30	34.16	33.32	30.36
Pr	3.45	2.50	3.17	5.59	1.18	4.88	3.65	4.16	4.31	3.08	7.60	3.36	4.03	3.99	4.05	4.15	3.96	3.31	4.20	3.89	3.30
Nd	14.73	11.88	14.51	23.68	5.33	19.01	13.70	16.38	17.07	14.26	28.37	13.07	14.78	15.15	15.70	15.85	15.23	12.73	15.88	14.55	11.59
Sm	3.60	3.38	4.03	5.82	1.45	4.07	3.03	3.64	3.58	3.99	6.09	2.74	3.01	3.13	3.42	3.22	3.33	2.74	3.23	2.90	2.14
Eu	1.28	1.21	1.38	1.72	0.57	1.15	0.83	1.20	1.16	1.33	1.50	0.90	0.81	0.87	0.97	0.92	0.89	0.67	0.95	0.85	0.53
Gd	4.19	4.07	4.84	6.92	1.93	4.79	3.42	4.01	4.04	4.58	6.84	3.09	3.45	3.44	3.83	3.51	3.77	3.02	3.61	3.29	2.31
Tb	0.72	0.70	0.86	1.16	0.37	0.78	0.55	0.61	0.61	0.83	1.11	0.48	0.54	0.56	0.61	0.53	0.60	0.49	0.55	0.50	0.31
Dy	4.32	4.25	5.16	6.90	2.51	4.41	3.28	3.37	3.38	5.07	6.42	2.67	3.21	3.21	3.52	3.03	3.46	2.91	3.06	2.77	1.73
Ho	0.95	0.94	1.14	1.48	0.58	0.95	0.71	0.72	0.70	1.11	1.43	0.54	0.68	0.69	0.74	0.64	0.71	0.61	0.63	0.60	0.35
Er	2.59	2.57	3.11	4.13	1.63	2.66	2.00	1.89	1.85	3.15	3.91	1.49	1.94	1.94	2.00	1.76	1.99	1.70	1.74	1.74	0.98
Tm	0.41	0.40	0.50	0.66	0.27	0.41	0.31	0.31	0.28	0.49	0.61	0.23	0.30	0.31	0.31	0.28	0.32	0.27	0.28	0.26	0.15
Yb	2.62	2.54	3.29	4.17	1.70	2.61	2.04	1.86	1.70	3.13	3.89	1.41	1.99	1.98	1.98	1.73	2.01	1.71	1.81	1.71	1.00
Lu	0.42	0.37	0.50	0.64	0.27	0.41	0.30	0.28	0.26	0.50	0.61	0.21	0.31	0.29	0.29	0.27	0.29	0.26	0.27	0.27	0.15
Hf	2.81	2.19	3.02	4.27	0.79	3.65	2.28	3.13	2.92	3.01	5.10	2.29	2.76	2.60	2.61	2.50	2.58	2.03	2.55	2.43	1.54
Ta	0.52	0.66	0.49	1.12	0.17	0.79	0.47	0.80	0.53	0.47	1.26	0.74	0.52	0.68	0.51	0.68	0.81	0.43	0.64	0.78	0.59
Pb	2.64	20.07	2.51	20.76	2.56	2.77	3.75	2.71	2.91	2.45	4.62	3.88	2.63	3.39	3.06	2.79	2.70	2.47	2.83	2.62	2.24
Th	1.04	0.49	0.75	2.37	0.32	2.74	2.63	1.51	1.37	0.72	4.60	1.25	3.18	2.76	2.47	3.52	2.64	2.47	3.63	2.76	4.21
U	0.24	0.13	0.18	0.54	0.08	0.51	0.70	0.28	0.25	0.16	0.83	0.24	0.77	0.71	0.62	0.76	0.65	0.64	0.78	0.65	0.85
ΣREE	74.75	56.99	72.69	123.39	28.07	103.93	77.41	88.58	89.69	70.77	162.77	71.14	84.94	84.90	85.82	85.19	85.29	70.88	87.05	83.57	71.22
Eu/Eu*	1.01	1.00	0.96	0.83	1.04	0.79	0.79	0.96	0.93	0.95	0.71	0.94	0.77	0.81	0.82	0.83	0.77	0.71	0.85	0.85	0.72
$(La/Sm)_N$	1.94	1.18	1.39	2.03	1.34	2.94	2.99	2.90	3.00	1.37	3.26	3.12	3.54	3.34	2.97	3.26	3.08	3.11	3.34	3.78	4.93
$(Gd/Yb)_N$	1.32	1.33	1.22	1.37	0.94	1.52	1.39	1.78	1.97	1.21	1.45	1.81	1.44	1.44	1.60	1.68	1.55	1.46	1.65	1.60	1.91
$(La/Nb)_{PM}$	1.70	1.17	1.47	1.61	1.62	1.75	2.94	2.14	2.22	1.45	1.83	2.21	2.94	3.02	2.80	3.17	2.87	2.93	3.27	3.55	3.33

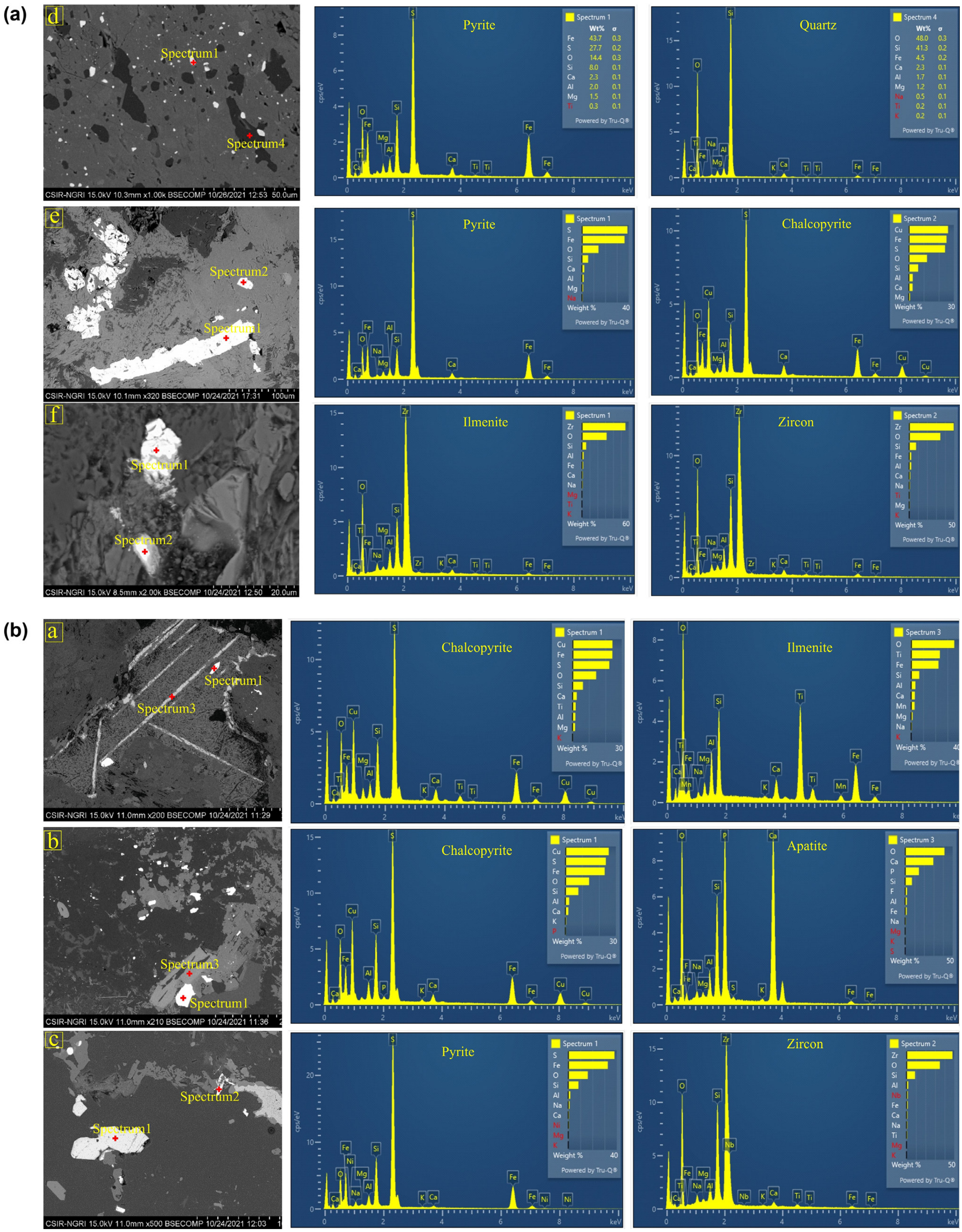

Fig. 4. Scanning electron microscopic (SEM) images of opaque and accessory minerals. Back-scattered electron (BSE) photograph with spectrum image showing chalcopyrite (a, b), ilmenite (a), apatite (b), pyrite and zircon (c) in sample OP-72–05; pyrite and quartz (d) in sample OP-81–05; pyrite and chalcopyrite (e) in OP-83–05 and ilmenite and zircon (f) in OP-84–05.

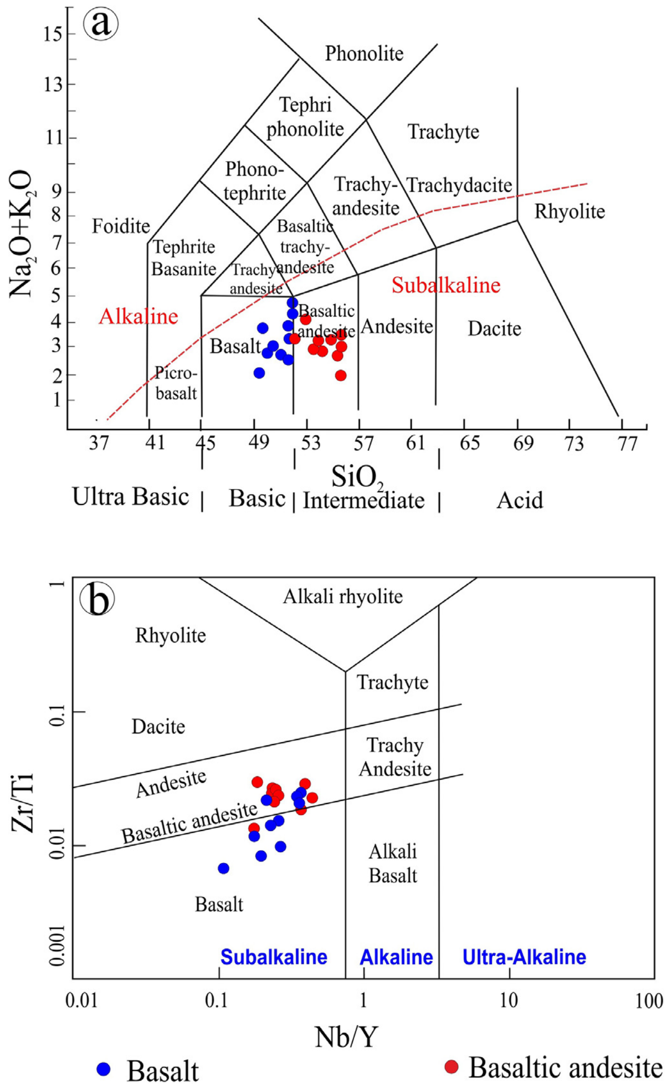

Fig. 5. (a) Total alkalis–silica diagram (Le Bas et al., 1986). Values of major oxides are on 100% anhydrous basis (Verma et al., 2002, 2003). Sub-alkaline and alkaline fields are after Irvine and Baragar (1971) which is demarcated by red dashed line. (b) Zr/Ti vs. Nb/Y plot (after Pearce, 1996) indicating subalkaline nature of the studied volcanics.

are mentioned on the individual images. EDS spectra were also obtained for one minute counting time with 15 kV accelerating voltage, a number of counts obtained for individual analysis were mentioned on the individual spectra. Minerals phases identified through SEM studies is discussed in the subsequent section.

4. Results of petrographic and SEM studies

As discussed in subsequent sections, detailed petrographical and geochemical studies on Bonai volcanics, indicate lithological variations from basalt to basaltic andesite. These samples are medium to fine-grained and composed mainly of plagioclase and pyroxene as primary minerals and amphiboles, sericite, epidote, and chlorite as secondary minerals (Fig. 3a) and ilmenite as an accessory mineral. They are inequigranular and show an overall porphyritic texture with the groundmass comprising plagioclase, clinopyroxene (Fig. 3a, d, e, h, i), and volcanic glass (Fig. 3b, e). Plagioclase is the dominant phenocryst phase with pyroxene and amphiboles (Fig. 3d). The presence of saussuritized plagioclase (sample OP-84/05) and secondary amphiboles indicate that these rocks were affected by hydrothermal alteration, which is also corroborated by the presence of skeletal and relict pyroxene (OP-87/05; Fig. 3c, d). The process of uralitization, which involves the formation of amphiboles from pyroxene, can also clearly be seen from the sample OP-91/05 (Fig. 3d). Further, some samples contain glass within the angular spaces between the primary minerals that show intersertal texture (Fig. 3b, e). In addition, some of the thin sections have demonstrated the presence of silica in voids (OP-75/5, Fig. 3b). Myrmekite texture is also seen in the few thin sections (Fig. 3g, h), indicating possible metasomatic alteration. Similarly, the ophitic texture is preserved in some thin sections (Fig. 3i).

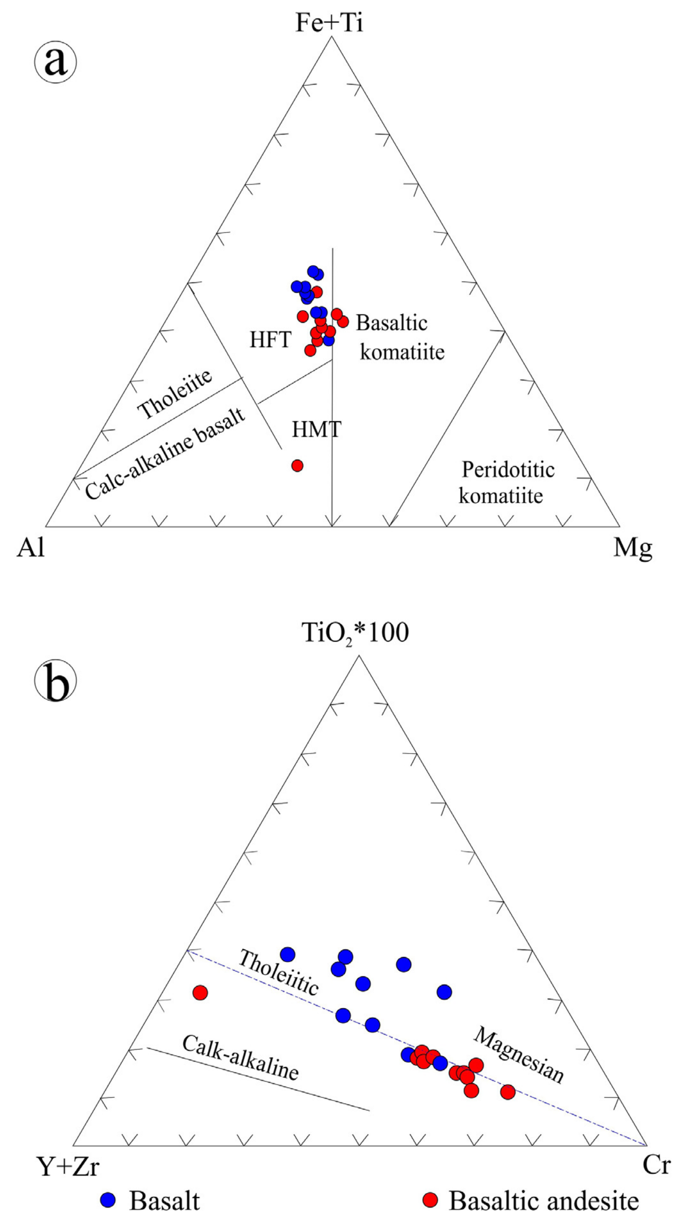

Fig. 6. (a) Jensen cation plot between Fe+Ti-Al-Mg (after Jensen, 1976) for Bonai volcanics. HFT: high iron tholeiite, HMT: high magnesium tholeiite. (b) Ternary plot ($TiO_{2\times}100$-($Y + Zr$)-Cr) (after Davies et al., 1979) illustrating tholeiitic affinity with magnesium enrichment trend for the studied volcanics.

SEM was used to identify the different mineral phases, specially altered mineral phases and opaque minerals in the studied rocks. These rocks are mainly composed of clinopyroxene and plagioclase as major rock-forming minerals. The accessory mineral phases are identified as chlorite, apatite, epidote, sericite and opaque minerals. These rocks generally show sub-ophitic textures. The chlorites and uralites are found as altered clinopyroxenes while the sericite

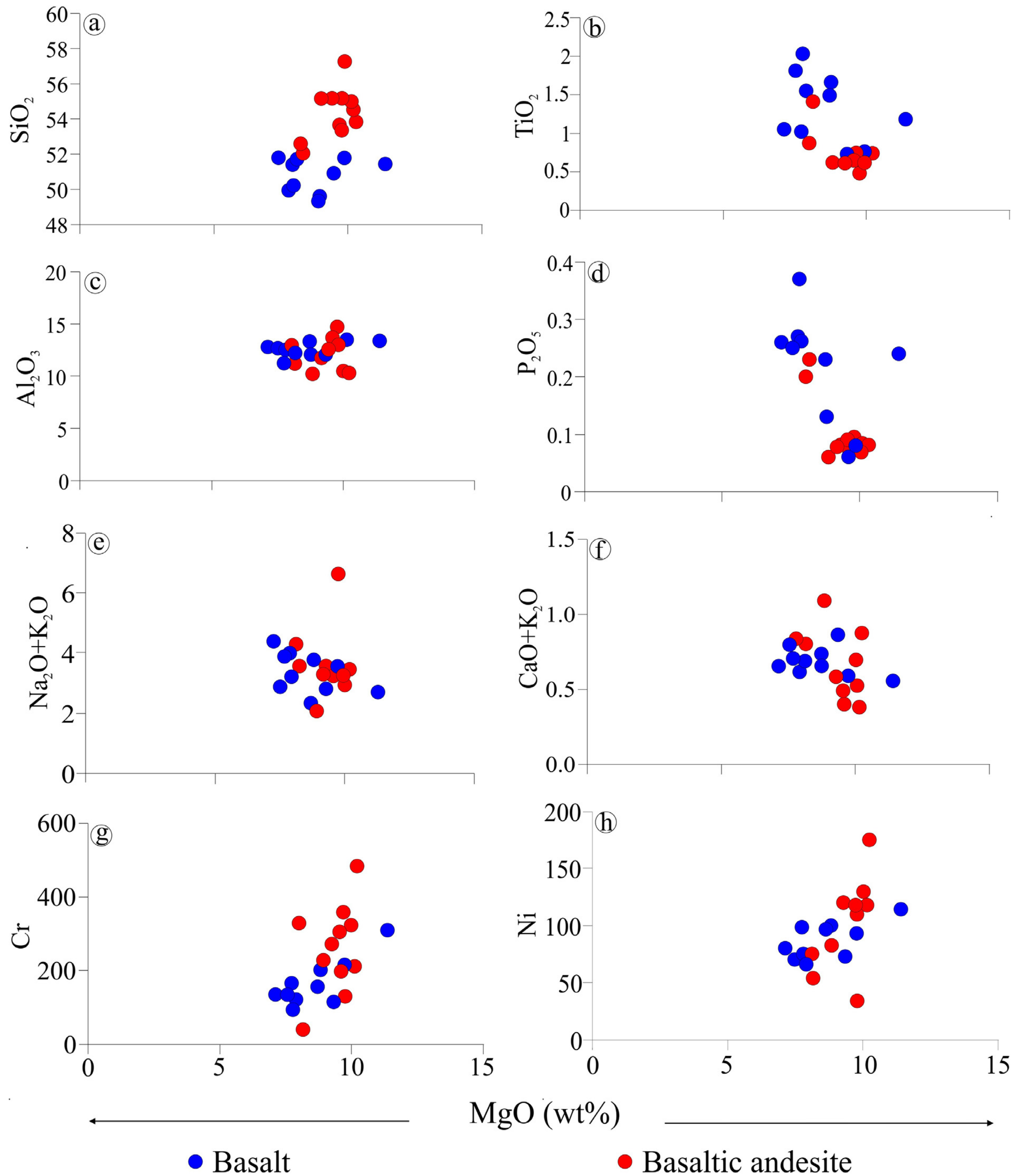

Fig. 7. Harker diagram for the major and trace elements of Bonai volcanic rocks.

and epidotes are observed within the large plagioclase grains. The opaque minerals pyrite, chalcopyrite, and accessory minerals apatite, zircon and ilmenite respectively, were also identified with the help of this study which are shown in Fig. 4.

5. Geochemistry

5.1. Major and trace elements

The studied rocks are characterized by a moderate range of SiO_2 (49.35–57.81 wt%), Al_2O_3 (10.21–14.68 wt%), Fe_2O_3 (2.20–15.82 wt%), CaO (5.14–11.15 wt%), TiO_2 (0.48–2.03 wt%) with moderate to high contents of MgO (7.14–11.39 wt%). The alkali contents are up to 6.72 wt% (Table 1). In addition, transition metals like Cr and Ni range from 32 to 483 ppm and 34–175 ppm, respectively (Table 2). These basalts and basaltic andesite exhibit sub-alkaline character (Fig. 5a), which is also substantiated by the Zr/Ti vs. Nb/Y plot (Fig. 5b). The majority of the samples lie in the field of high-iron tholeiites (HFT) (Fig. 6a) and also exhibit magnesium enrichment trend in $TiO_{2\times}100$-(Y + Zr)-Cr plot (Fig. 6b) (Davies et al., 1979). Furthermore, some of the samples in Fig. 6a share the boundary with basaltic komatiites, how-

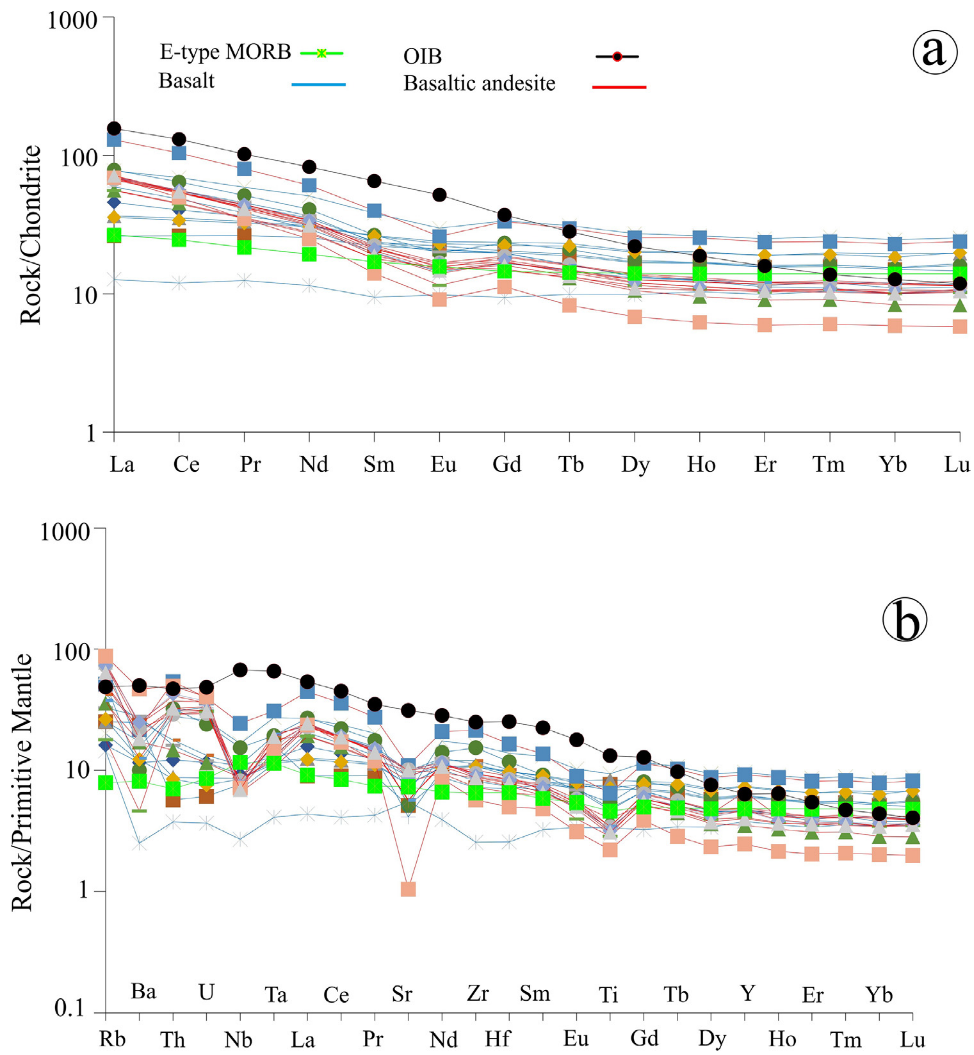

Fig. 8. Chondrite normalized REE (a) and primitive mantle-normalized (b) elemental patterns for Bonai volcanic rocks. Chondrite values are from Sun and McDonough (1989).

ever, they are devoid of spinifex texture and hence cannot be termed komatiites (Arndt et al., 2008). In addition, they exhibit wide range of Mg# (100 $Mg^{2+}/(Mg^{2+} + Fe^{2+})$ from 50.50 to 89.80. The presence of normative hypersthene (Table 1) in the CIPW normative compositions (Middlemost, 1989) indicate their tholeiitic nature. Furthermore, the calculated Differentiation Index (D.I.) (normative quartz (Q) + orthoclase (Or) + albite (Ab) + nepheline (Ne) + kalsilite (Ks) + leucite (Lc)) of 25.62 to 46.29 (Table 1), would indicate moderate to a high degree of differentiation of the primary melt (Thornton and Tuttle, 1960). Similarly, Solidification Index (S.I.) (100 × {MgO/(MgO + FeO + Fe_2O_3 + Na_2O + K_2O)}) (Kuno, 1964) that range from 26.58 to 49.25 (Table 1), suggest involvement of fractional crystallization during the time of its evolution. In addition, a positive correlation of MgO with Cr and Ni and a negative correlation with Cao, Na_2O, P_2O_5, and TiO_2 (Fig. 7) suggest magmatic differentiation controlled by fractional crystallization. The enriched to depleted concentrations of LILE, HFSE, and variable negative and positive anomaly at Nb and Ta (Fig. 8a, b) is the characteristic feature of these rocks. Further, LREE/HREE (La/Yb_N: 1.27–11.75), LREE/MREE (La/Sm_N: 1.18–4.93), and MREE/HREE (Gd/Yb_N: 0.94–1.97, Dy/Yb: 0.99–1.33) and low $(Nb/La)_{PM}$: 0.28–0.85, relatively high $(La/Nb)_{PM}$: 1.17–3.55 (Fig. 8a, b) ratios would suggest moderate fractionation and enrichment in LREE. The Eu anomaly (Eu/Eu*) ranges from 0.71 to 1.04, showing minor negative Eu anomaly on chondrite-normalized REE diagram (Fig. 8a).

6. Discussion

6.1. Alteration and element mobility

Megascopically chosen hand specimens do not show the effect of alteration or presence of secondary veins. However, the formation of sericite over the plagioclase grains (Fig. 3a), presence of skeletal (Fig. 3c), and relict pyroxene (Fig. 3d) suggest an alteration in these rocks. HFSE and REEs generally get least affected by the post magmatic alteration unless they undergo high-grade metamorphism. Therefore, these elements are widely used to understand the mantle melting processes and the source of the melt (Song et al., 2006). These largely immobile elements (Polat and Hofmann, 2003) are also considered a proxy to evaluate the extent of mobility. It can be seen from Fig. 9 that Zr shows a good correlation with selected HFSE and REEs. It suggests that these elements remained largely unchanged during the post-magmatic alteration, as corroborated by Fig. 8a, b. The calculated AI (Alteration Index) value of these rocks between 40 and 69 (Table 1) would also indicate them to be unaffected by strong alteration (Ishikawa et al., 1976; Large et al., 2001).

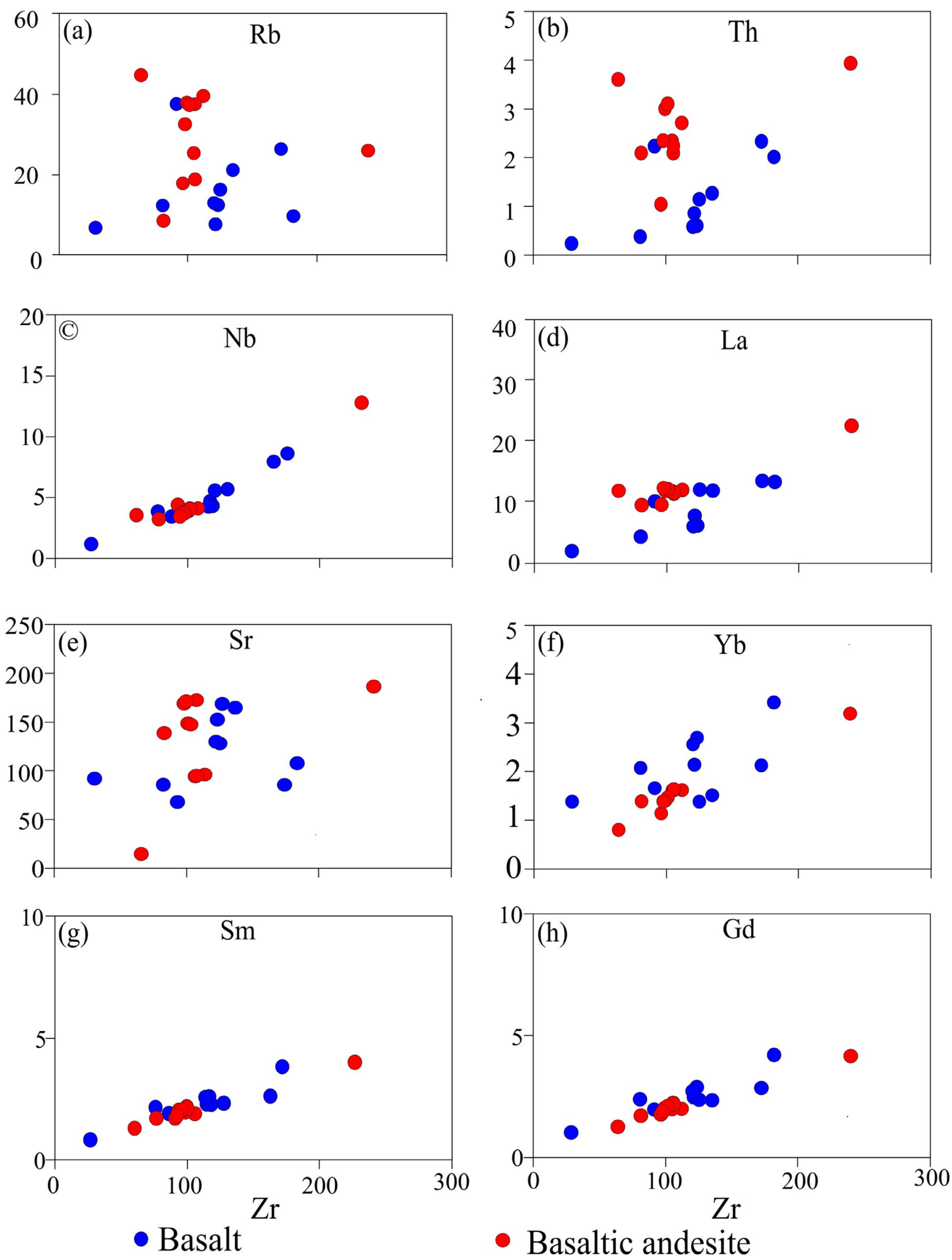

Fig. 9. Correlation of selected LILE, HFSE and REE against Zr, indicating possible mobilization of elements due to hydrothermal alteration in the investigated samples. The linear trends (Fig. 8c-h) indicate that these samples are cogenetic and not much affected by hydrothermal alteration.

6.2. Fractional crystallization

Fractional crystallization serves as a critical differentiation mechanism in the evolution of basaltic magma. We interpret the evolution of investigated samples in terms of magmatic differentiation controlled by fractional crystallization. The positive correlation of MgO with Cr and Ni and negative with Al_2O_3 and Na_2O_3 (Fig. 7) indicates the involvement of fractional crystallization in their genesis. Similarly, variable content of Ni (34–175 ppm), Cr (32–483 ppm) and Mg# (50.50–89.80) indicate their primitive to evolved nature which is ascribed to the varying extent of fractional crystallization. (Zeng et al., 2018; Pahari et al., 2019). Comparatively, the lower content of Ni than Cr in these samples (Table 2) may be attributed to the high partitioning coefficient of the ele-

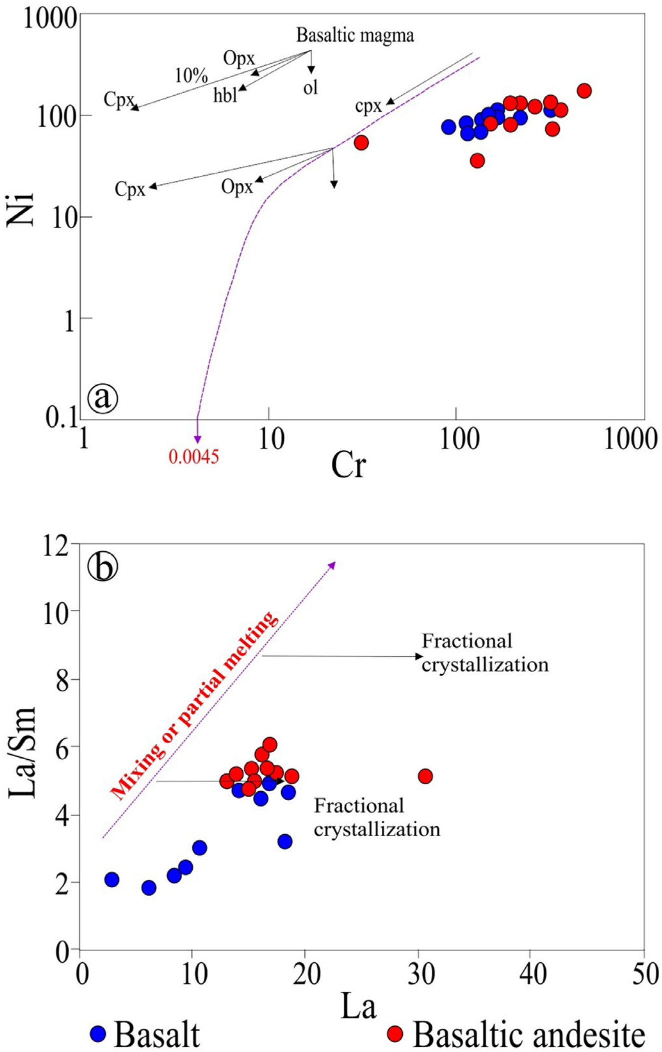

Fig. 10. Discrimination diagram representing the possible fractional crystallization process in Bonai volcanic rocks. (a) Ni vs. Cr plot; partition coefficients value is taken from Rollinson (2014). (b) La/Sm vs. La plot, which clearly indicates that fractional crystallization played a key role in the generation of Bonai volcanics. Mineral fractionation trends are from Xia et al. (2015).

ments present in the early phase of crystallizing minerals olivine and orthopyroxene, which have had resulted in rapid depletion of Ni (Arndt et al., 2008). The variable CaO content with respect to MgO (Table 1) could imply the presence of CaO-MgO (clinopyroxene) and CaO rich (plagioclase) minerals in addition to MgO-rich minerals. The Eu/Eu*: 0.71 to 1.04 ratio rules out the possibility of the major role of plagioclase fractionation; however, Cr vs. Ni and La vs. La/Sm plots (Fig. 10a, b) do indicate the role of fractional crystallization to some extent in the genesis of Bonai volcanics. The minor negative Eu anomaly and negative Sr anomaly (Fig. 8a, b) of the investigated rock with presence of significant plagioclase can be best explained by decreasing $^{plagioclase/melt}D_{REE}$ values with rising H_2O content in the magma and drop of pressure (Bedard, 2006). In studied samples, plagioclase is present, but correspondingly Eu anomaly is insignificant. Moreover, a distinct trough at Sr is a possible consequence of low-pressure plagioclase fractionation controlled by pressure-sensitive $^{plagioclase/melt}D_{Sr}$ values (Bedard, 2006). Therefore, these distinct trace elements and REE signatures of the plagioclase-rich Bonai volcanics, manifested in terms of negative Sr anomalies and small negative Eu anomalies respectively, also reflect their evolved character, pressure-sensitive crystallization of plagioclase and variations in meltwater content during crystallization.

6.3. Crustal contamination

The mantle-derived magmas generally undergo crustal contamination due to variable degrees of crustal assimilation during their ascent through the crust (Ghosh et al., 2019). However, their incompatible elements and ratios largely remain unaffected when the primary melt is not significantly contaminated with crustal components. The involvement of crustal material in contamination will result in higher Th/Yb, Th/Sm, Zr/Y and Zr/Yb ratios as the continental crust contains higher contents of Zr and Th relative to Sm, Y and Yb (Taylor and McLennan, 1985). The geochemical constituent like high Al_2O_3, associated positive Rb and Th anomalies, negative Ba, and Ti anomalies, minor Nb depletion relative to La on the primitive mantle- normalized multi-element diagrams (Fig. 8a, b) indicate the effects of contamination from the crustal component in the evolution of Bonai volcanics. Moreover, an inconsistent pattern of LILE and no significant negative HFSEs anomaly except minor trough at Nb and Sr relative to La (Fig. 8a, b), can also be explained by crustal contamination (Huppert and Sparks, 1985; Rudnick and Gao, 2003; Song et al., 2008; Lai et al., 2012; Rasheed et al., 2021) rather subduction which is characterized by prominent depletion of Nb and Ta. Further, to visualize the effect of contamination, we utilized the REE and HFSE correlation plot (Fig. 11a, b), where the majority of investigated samples lie away from the normal mantle ratios suggesting widespread crustal contamination of these volcanics, which is also corroborated by lower $(Nb/La)_{PM}$: 0.28–0.85, $(Nb/Th)_{PM}$: 0.14–1.35 and $(Th/Nb)_{PM}$: 0.74 –6.95 ratios (Polat et al., 1999; Simonov et al., 2014). Furthermore, an inconsistent pattern of LILE and no significant negative anomaly of HFSEs (Fig. 8a, b), except minor trough at Nb and Sr, can be ascribed in terms of crustal contamination (Rudnick and Gao, 2003; Van Hunen and Moyen, 2012; Rasheed et al., 2021) which is also in concurrence with Nb/Yb vs. Th/Yb and La/Ta* vs. La/Sm plots (Fig. 11c, d). In addition, Nb/ La and La/Nb vs. SiO_2 plots (Fig. 12a, b) indicate the involvement of assimilation with fractional crystallization (Dong et al., 2010) for the studied samples. It is thus evident that the magma may have undergone fractional crystallization, assimilation, and crustal contamination during its ascent to the surface.

6.4. Mantle melting and source

REE and incompatible elements are extremely sensitive to the degree of mantle melting and thus provide information about the nature of the melt (He et al., 2010; Manikyamba et al., 2015). Therefore, the REE pattern and incompatible trace element ratios are often used to understand such processes (Rajesh et al., 2013; Teng and Santosh, 2015). The distinctly parallel REE patterns shown by the Bonai volcanic rocks (Fig. 8) point to their extraction from a similar mantle source. HREEs, specifically Yb and Lu, have high garnet/melt partition coefficient, thereby making them compatible with garnet but incompatible with spinel, whereas La, Sm, and Gd have low garnet/melt partition coefficients and thus are incompatible with garnet (Rollinson, 1993; Farmer, 2014). Similarly, REE ratios like La/Yb, Sm/Yb, Dy/Yb, and Gd/Yb show strong fractionation in the melt generated in the garnet stability field, whereas slightly fractionated La/Yb and nearly unfractionated Sm/Yb, indicate mantle melting in field of spinel peridotite (Xu et al., 2005; Lai et al., 2012; Davidson et al., 2013). To validate the source and extent of melting, the La/Yb vs. Dy/Yb (Fig. 13a) and Sm vs. Sm/Yb (Fig. 13b) plots are utilized where it is observed that the majority of the samples lie within the spinel lherzolite field (Fig. 12a) and generated by 5–10% melting (Fig. 13b).

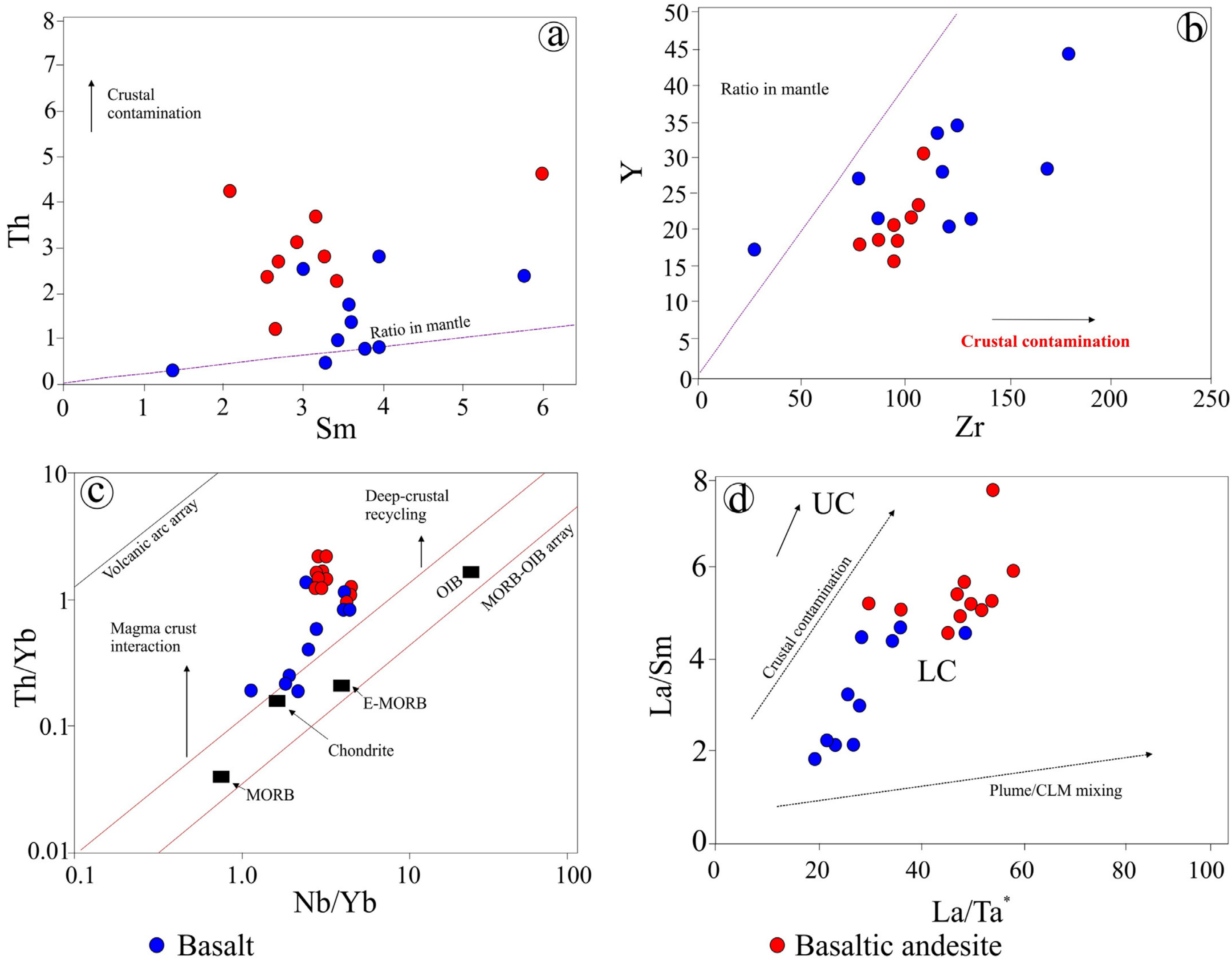

Fig. 11. (a) Sm vs. Th and (b) Zr vs. Y plots (Ghosh et al., 2019) exhibiting the effect of crustal contamination in the studied rocks. (c) Nb/Yb vs. Th/Yb plot (after Pearce, 2008), demonstrating the trend in Bonai volcanic samples which plot towards higher Th/Yb ratios away from the oceanic MORB-OIB array. This plot also suggests the role of lithospheric mantle and magma-crust interactions in the genesis of parent magma. (d) La/Ta* vs. La/Sm plot (after Lassiter and DePaolo, 1997) showing crustal contamination and lower crustal affinity. Ta* = Nb/17. UC: upper continental crust; LC: lower continental crust.

In addition, the combination of REE and incompatible elements, like Zr, Nb, Yb, and Y, are also usually used to understand the tectonic setting for melt generation. Thus, we plot the Zr/Y vs. Nb/Y diagram (Fig. 14a), where they occupy the field of oceanic plateau basalt having mantle plume affinity (Fig. 14a). Further, the Th/Yb: 0.19–4.22, Zr/Y: 1.65–6.35 are comparable with NMORB values; however, in the Zr/Yb vs. Nb/Yb correlation, these samples mostly cluster around E-MORB (Fig. 14b), which is also supported by Zr/Sm (19.82–42.33) ratios of the Bonai volcanics which are greater or close to that of the primitive mantle (Zr/Sm: 25) (Frey et al., 1980; Menzies et al., 1991). Additionally, the Zr/Ba (0.20–2.52), Zr/Hf ratio (36.07–47.20) and La/Nb ratio (1.13–3.43), indicate the genesis of parental melt from asthenospheric sources and metasomatic enrichment respectively (Menzies et al., 1991; Greenough et al., 1998; Kurkcuoglu, 2010). We thus infer that the Bonai volcanics have resulted from the interaction of plume melts with a metasomatized subcontinental lithospheric mantle (SCLM) and crustal component before their ascent and emplacement at the surface.

6.5. Mantle potential temperature

We have calculated mantle potential temperature and pressure for the samples having MgO > 8.0 wt% from the Fractionate PT (Fig. 15). FRACTIONATE PT thermobarometers (Lee et al., 2009) uses magma Si and Mg concentrations to determine basaltic magma pressures and temperatures. To determine the composition of the primary magma, this program considers primitive basalts that have fractionated along olivine-control lines and reverse-fractionates the olivine crystallization (or accumulation for picrites) process. The program then calculates the average pressures and temperatures of melt segregation from the mantle, assuming that these magmas emanated from a peridotitic source (Ol + Px). For polybaric melting, the calculated T and P would signify the T and P of the accumulated aggregate melt. To calculate the T_p, the K_D (partition coefficient) for three studied samples is taken 1, the K_D for (Fe/Mg) Ol/(Fe/Mg) is taken as 0.32, and fO_2 is molar Fe^{III}/Fe^T. The barometer has an uncertainty of ±0.20 GPa whereas, the uncertainties in temperature are ±3% (corresponding to ~40 °C for

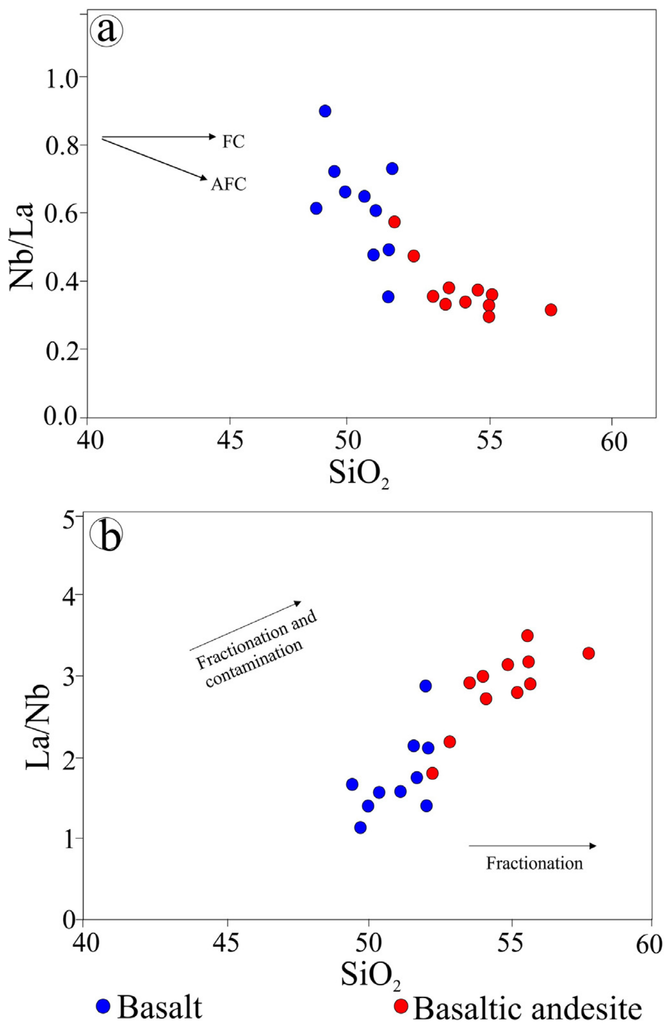

Fig. 12. SiO_2 vs. Nb/La (a) and SiO_2 vs. La/Nb (b) plots for Bonai volcanics suggesting the involvement of fractional crystallization in genesis of these rocks (Dong et al., 2010).

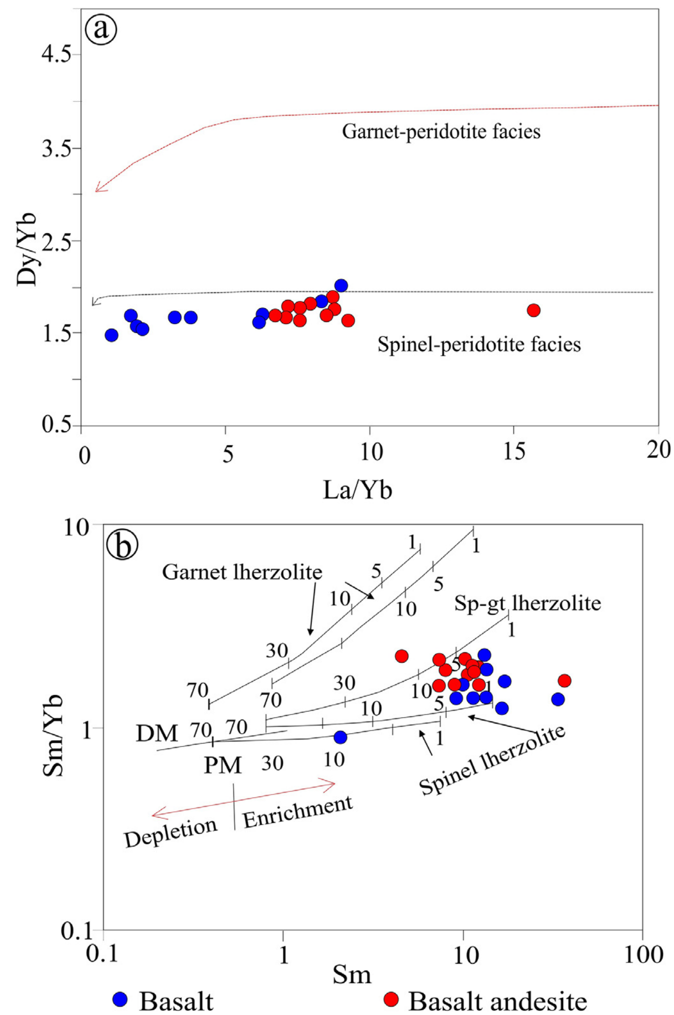

Fig. 13. (a) Dy/Yb vs. La/Yb and (b) Sm vs. Sm/Yb plots (after Zhao and Zhou, 2007) for the studied volcanic rocks indicating magma generation in spinel peridotite stability field with 5–10% melting of spinel lherzolite. Melting curves are after Aldanmaz (2002). DM: depleted mantle; PM: primitive mantle. Mode and melt mode curve for spinel and garnet are taken from Kinzler (1997) and Walter (1998) respectively.

a temperature of 1400 °C). The calculated T_p of around 1340–1600 °C with corresponding pressure of 0.5 to 3.5 GPa of these volcanics, suggest strong crust-mantle thermal interaction due to the decompressive melting of the plume head at the crust-mantle level.

Similarly, we have also calculated primary magma composition for 3 samples (OP 91/05, OP 72/05, OP 78/05) which met the criteria of PRIMELT3. This software (Herzberg and Asimow, 2015) models both batch and accumulated fractional melting, using hybrid forward and inverse models to incrementally add or subtract olivine from an evolved lava composition until a melt fraction is generated, which is capable of (i) being formed by partial melting of mantle peridotite, and (ii) replicates the major element composition of the starting magma through fractionation or accumulation of olivine. It is also equipped to calculate the degree of partial melting and mantle potential temperature (T_P) required to generate primary magma from a more evolved magma composition. For all the investigated samples, $Fe^{2+}/\Sigma Fe$ and Fe_2O_3/TiO_2 ratios in the mantle peridotite were kept at 0.88 and 1, respectively. The calculated mantle potential temperatures from the PRIMELT3 (batch melting) range from 1576 °C to 1696 °C, which is relatively higher than that obtained from Fractionate PT thermobarometer. The total uncertainty in T_p calculated by PRIMELT3 is ±60 °C (2 sigma) (Herzberg and Asimow, 2015). Primary magma compositions, degree of melting, forsterite content of olivine in equilibrium with the melt, and other related details are given in Table 3.

We find that the primary magmas of the studied rocks were generated around pressure reaching up to 3.5 GPa (Fig. 15) and T_p of around 1300–1700 °C. Our estimated temperatures are higher than 1200–1500 °C of the parental magma of Bonai volcanics as reported by Banerjee et al. (2016), which may be due to relatively lower contents of FeO and MgO in their studied samples. The lower values of pressure of a few samples (Fig. 15), indicates shallow depth of emplacement. The association of such high mantle potential temperature can be constrained in terms of decompression melting of the mantle plume head below the crust, whose initial temperatures may have been higher by 150–200 °C than that of the ambient mantle (Wolfe et al., 1997; Desharnais, 2005; Herzberg and Asimow, 2008; Cao et al., 2011).

In similar studies, Korenaga (2008) proposed that the mantle initially increased in temperature from ~1650 °C at 4.5 GPa to ~1700 °C at 3.6 GPa, subsequently followed by rapid cooling to the present-day value of 1350 °C. Subsequently, Davies (2009) pro-

Table 3
Primary magma compositions for Bonai volcanics (Singhbhum Craton), calculated by PRIMELT for the batch melting. Tp (°C) is mantle potential temperature (method of Herzberg and Asimov (2015). Degree of melting (F%), forsterite content of olivine in equilibrium with the melt (Fo), percentage of olivine added to the sample composition in order to obtain primary magma composition (Ol%).

Sample No.	SiO_2	TiO_2	Al_2O_3	FeO^T	MnO	MgO	CaO	Na_2O	K_2O	P_2O_5	Tp (°C)	Fo	F%	Ol%
OP 91/05	47.29	0.43	7.07	9.50	0.17	26.85	6.15	1.38	0.24	0.05	1696.00	94	53	56.43
OP 72/05	48.74	0.55	8.08	9.35	0.15	24.00	5.54	1.94	0.65	0.13	1646.97	94	46	48.95
OP 78/05	52.62	0.47	7.62	8.15	0.13	20.26	8.36	1.20	0.31	0.04	1576.84	94	51	32.67

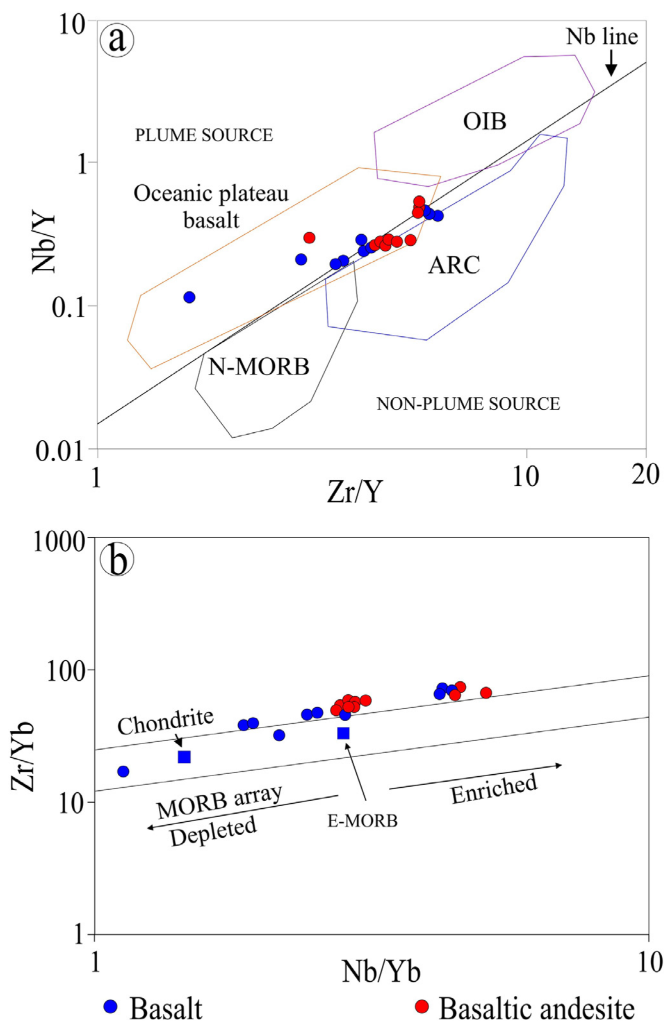

Fig. 14. (a) Zr/Y vs. Nb/Y plot (after Condie, 2005). Bonai volcanics plot in oceanic plateau basalt field, suggesting plume affinity. (b) Zr/Yb vs. Nb/Yb plot where the studied samples plot close to E-MORB field. Data source: Chondrite, E-MORB- Sun and McDonough (1989); depleted mantle (MORB data)- Salters and Stracke (2004).

vided a secular cooling model, indicating a constant decrease of temperature from 1800 °C at 4.5 GPa to a modern-day temperature of 1300 °C. Our recent investigation (Jafri et al., 2021) also reported a similar mantle potential temperature of around 1630–1660 °C for Paleoarchean ferropicrite and ferrobasalt of the Jojohatu area in the north Singhbhum Craton, which was generated by a mantle plume. Higher T_p of parental magma for the Bonai volcanics (1300 to 1700 °C) with pressure reaching 3.5 GPa (Fig. 15), would thus conform with magma generation from a mantle plume.

6.6. Tectonic evolution

There have been suggestions that many volcanic suites of this craton may have a subduction-related affinity during the Archean-Paleoproterozoic period (Alvi and Raza, 1991, 1992; Raza et al., 1995; Sengupta et al., 1997; Manikyamba et al., 2015, 2020; Banerjee et al., 2016; Singh et al., 2017), including the presently studied Bonai volcanics (Manikyamba et al., 2017). The precise time frame, however, remains unresolved. In comparison, recent studies of Arif et al. (2021), Rasheed et al. (2021) as well as our study over the Jojohatu volcanics in the northern part of the IOG (Jafri et al., 2021) indicate mantle plume affinity. In addition, the Nb/Y-Zr/Y plot (Fig. 14a) for the studied samples, suggests that almost all of them occupy the field of oceanic plateau basalt and oceanic subduction unrelated settings (Fig. 16a). Moreover, the HFSE/LILE ratios and enriched signature (Fig. 16b) for these volcanics indicate the involvement of the asthenosphere in the melt generation. This can be explained in terms of partial melting of a depleted mantle source and heterogenous enrichments by sub-continental lithospheric and crustal components. The mixing of depleted asthenosphere melt with OIB type melt can produce enriched geochemical signatures during the extensional thinning caused by the hot mantle plume. Importantly, we have not found any prominent subduction-related signatures in these volcanics. The variable Nb and Ta, along with positive Rb and Th, negative Ba, and Ti anomalies, can be explained by possible contamination as discussed above. Further, the higher estimated mantle potential temperature (1300 to 1700 °C) can only point to a mantle plume source and not subduction generated magmas.

6.7. Support from geophysical studies

Evidently, the Singhbhum Craton is associated with unusual geophysical signatures, unlike most of the other Indian, as well as global cratons (Pandey, 2020). The only comparable terrain as per our present-day knowledge could be the eastern block of the North China craton (Vasanthi and Santosh, 2021 and references therein). For example, this craton is associated with high velocity mafic crustal exhumation (Fig. 17), positive gravity anomalies, especially in the volcanic terrains (Fig. 18), and an extremely thin lithosphere of only about 65–95 km due to persistent destruction of the lithospheric keel as revealed by heat flow (Negi et al., 1986, 1987; Pandey and Agrawal, 1999; Pandey, 2020), magneto-telluric (Shalivahan et al., 2014) and seismic receiver function (Kumar et al., 2013; Mandal, 2017). In comparison, in similar global terrains, the estimated lithosphere is extremely thick at around 250–350 km (Chapman and Pollack, 1977; Polat and Anderson, 1995; Pandey and Agrawal, 1999; Artemieva and Mooney, 2001; Pandey, 2016). The nature of geophysical anomalies would conform to large-scale mantle upwelling and crust-mantle thermal interaction. In such a scenario, the role of mantle fluids also becomes important, as revealed by elemental mobility and petrographic signatures. Bonai volcanics, sitting at the center of an uplifted prominent circular morphostructure

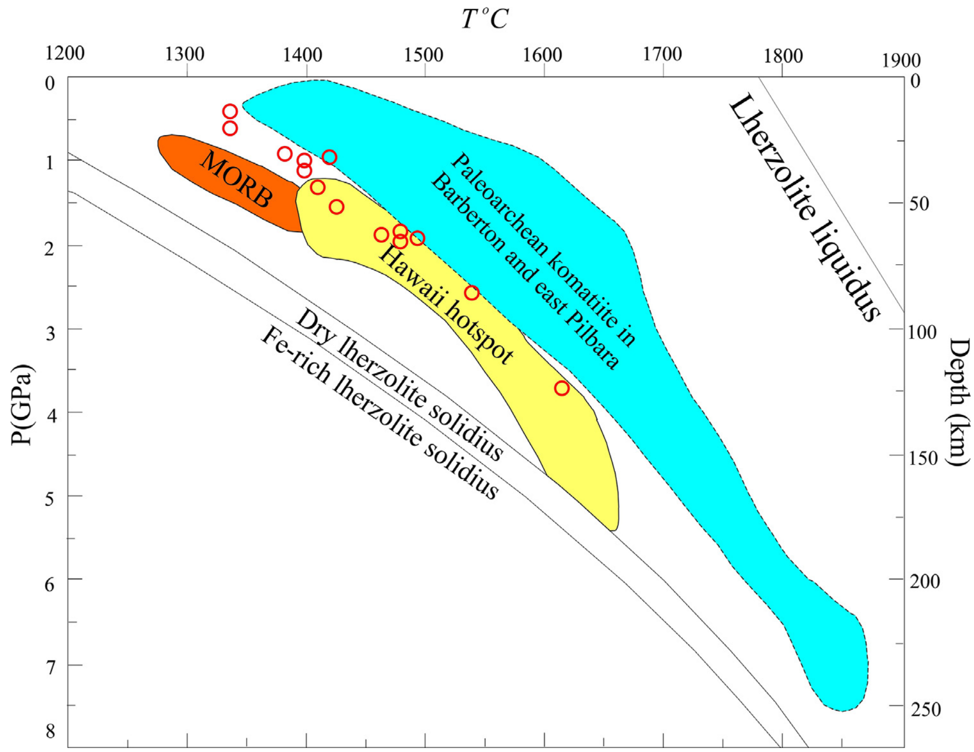

Fig. 15. Temperature-pressure plot (Lee et al., 2009) for Bonai volcanic samples having MgO > 8 wt%. Curved lines represent melting adiabats. The dry lherzolite solidus and liquidus are from Katz et al. (2003). The Fe-rich lherzolite solidus was estimated by lowering the dry lherzolite solidus by ~50 °C (Kushiro, 1996). The melting characteristics for MORB, Hawaii hotspot basalt and Paleoarchean komatiites, are from Lee et al. (2009) and Wang et al. (2019).

(Rantsman et al., 1995), is no exception. Effect of hydrothermal alteration and mantle metasomatism can be seen in many Bonai volcanic samples (Fig. 3c, d, g, h, i). Invariably, such alterations result in the lowering of velocities even in the highly denser mid to lower crustal rocks (Tripathi et al., 2012; Pandey et al., 2014, 2016).

6.7.1. Exhumation of mafic crust: seismic evidence

The crust-mantle seismic structure of the Singhbhum Craton and adjacent areas have recently been studied in detail by Mandal (2017), using fifteen 3-component broadband seismic network, which indicated the presence of a highly mafic (average Vs: 4.0 km/s, corresponding Vp, 7.0 km/s), heterogeneous and deformed crustal structure below Singhbhum Craton Fig. 17. shows the variation of computed Vp with depth (as obtained from averaged Vs of all the seismic stations using Vp/Vs as 1.75), together with the deduced crustal seismic structure underneath the Singhbhum Craton. This figure also includes similar data for the south Indian Shield (Pandey et al., 2013) as well as global shields and platforms (Christensen and Mooney, 1995) for comparison.

It is pertinent to note that the estimated crustal Vp obtained below this craton (Fig. 17), is much higher than recorded in the south Indian Shield and average global shields and platform. Noticeably, beneath this craton, the granitic-gneissic upper crust, as well the middle crust, is only about 2 km thick each, implying that the lower crust has exhumed to a depth of only 4 km from the surface, rest of the upper and middle crust being eroded. Further, the lower crust is underplated by a 14 km thick magmatic layer due to massive magma emplacement.

Another important feature which is revealed by Fig. 17 is the detection of a possible metasomatized zone between 14 and 30 km in which velocity drops down sharply from 3.93 km/s to 3.76 km/s. Metasomatism is a process that is caused by the interaction of the lower crust with mantle-derived hydrothermal fluids and halogens (Tripathi et al., 2012; Pandey et al., 2014, 2016). It is quite prevalent in mantle-plume-affected areas like Deccan traps (Pandey, 2020). It can lead to a drastic reduction in crustal velocities up to 15% (Pandey et al., 2016), as also revealed by Fig. 17. In Bonai too, the metasomatic alteration has been seen in quite a few samples (Fig. 3c, d, g, h, i).

Further, a close look at Fig. 17 indicates that the estimated velocities at four kilometres depth below Singhbhum Craton (below which lower crust is envisaged) is similar to the velocities recorded at a depth of 25–30 km in other global shields and platforms (Christensen and Mooney, 1995). It would mean that this craton is unusually mafic (avg. Vs: 4.0 km/s) and has exhumed by about 20 km or more. This is possible only if this craton interacted with a long-sustained mantle plume and in all likelihood not by subduction. Recorded P and T conditions (Sharma, 2009) would support this conjecture. It is compatible with the presence of thin lithosphere and positive gravity anomalies.

6.7.2. Gravity field

Bouguer gravity anomaly map of the Singhbhum Craton (Fig. 18), reveals a large variation in gravity anomalies from +10 mGal to about −60 mGal over the different geotectonic terrains. As this craton was subjected to several orogenic cycles in the past, its imprints can be seen in the form of gravity highs, which are generally associated with the synformal structures filled with metasediments (Iron Ore Group) and volcanics, likes, Dhanjori, Ongarbira, Dalma and Simlipal, over which Bouguer gravity anomalies reach as high as 0 to −5 mGal. In general, these volcanics/metavolcanic rocks have an average density of around 3.0 g/cm^3 or even more (Verma et al., al.,1978; Sarma, 1980).

In comparison, the Bonai volcanics, which is the area of the present study, is associated with variable gravity anomalies. Its western and southern parts, which are in direct contact or in

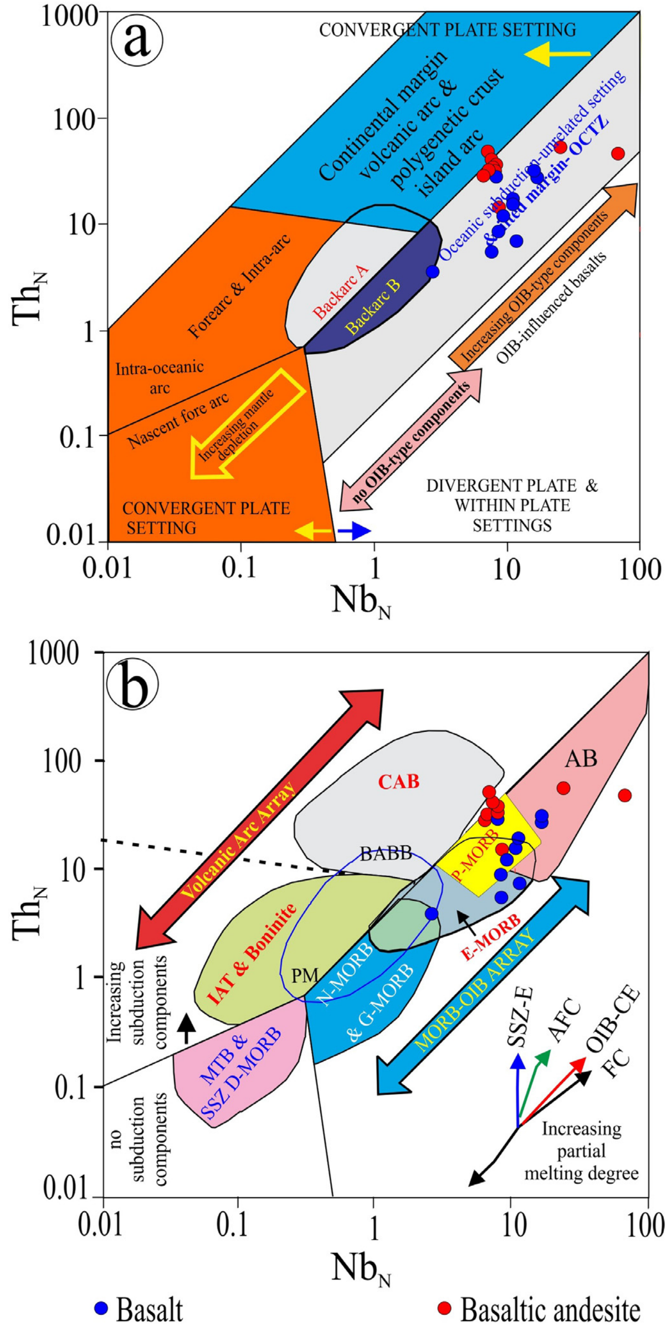

Fig. 16. Nb_N vs. Th_N plots (after Saccani, 2015) where the studied samples lie in the oceanic subduction unrelated setting-continent transition zone (OCTZ) (a), and in the field of P-MORB (b). Nb and Th values are normalized to the N-MORB composition (Sun and McDonough, 1989). Vectors in the plot represent the trends of compositional variations as a the major petrogenetic processes. FC: fractional crystallization; OIB-CE: ocean island type (plume-type) component enrichment; AFC: assimilation-fractional crystallization; SSZ-E: supra-subduction zone enrichment.

close association to IOG, are characterized by −10 to −30 mGal anomalies, while in its northern part, gravity anomalies reach −60 mGal, which can be attributed to the presence of thick low density (2.68 g/cm^3) Singhbhum granite/ granitoid basement complex underneath Fig. 19. shows a crustal density model along a profile AB, together with topographic variations, which runs across Bonai volcanic complex, Singhbhum granitic batholiths, and Simlipal volcanic suite. For the gravity modeling, we use the GM-SYS Profile Modeling Software (Geosoft Oasis Montaj, 2004), where the number of iterations with less RMS error provides the best-fit model. Initially, the layers and their insitu densities are fixed following seismic constraints and measured densities. In further iterations, the densities and layer thicknesses are changed in such a way that the calculated anomaly matches well with the observed field. The best fit between the observed and calculated gravity fields is obtained by minimizing the difference in a least-square sense. modeling results indicate that the Singhbum granitic region is bounded by deep faults on either side, as evidenced by the steepness of the gravity anomalies. This figure also reveals that over the volcanic terrains, the gravity field is distinctly positive. The high gravity field is accompanied by high elevations that exceed 700 m from the ambient at some places, which will conform to mantle plume-induced thermal uplifting. No other mechanism can possibly explain it. Measured high density of volcanic rocks (~3.0 g/cm^3), as mentioned earlier, would also indicate deep-level plume-induced melting of the magma source, which is in accordance with estimated mantle potential temperatures (1300 °C to 1700 °C). Subduction-associated volcanics would not be that dense.

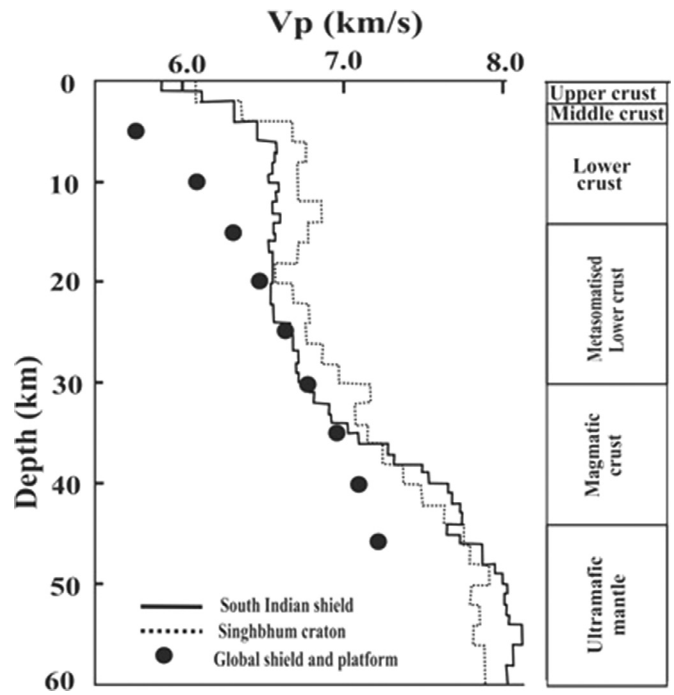

Fig. 17. Variation of computed Vp (as obtained from averaged Vs of all the seismic stations based on receiver function studies by Mandal (2017) and taking Vp/Vs: 1.75) with depth together with deduced crustal structure beneath the Singhbhum craton of eastern India. This figure also includes similar data for the south Indian shield (Pandey et al., al., 2013) as well as global shields and platforms (Christensen and Mooney, 1995) for comparison. The occurrence of considerable higher velocities beneath this craton compared to south Indian as well as global shields and stable platform, can clearly be seen.

7. Conclusion

The integrated geological, geochemical and geophysical studies over Bonai volcanics indicate that they are composed of basalt to basaltic andesites of tholeiitic nature. These volcanic rocks exhibit porphyritic texture and contain plagioclase feldspar and pyroxene as primary minerals and amphiboles, epidote, sericite and chlorite as secondary minerals. The accessory phases are mainly zircon, ilmenite, pyrite and chalcopyrite. They contain a moderate range of SiO_2 (47.94–53.77 wt%) and moderately high MgO (7.14–11.39 wt%) content. They have originated by magmatic differentiation and subsequent crustal contamination due to the decompressive melting of

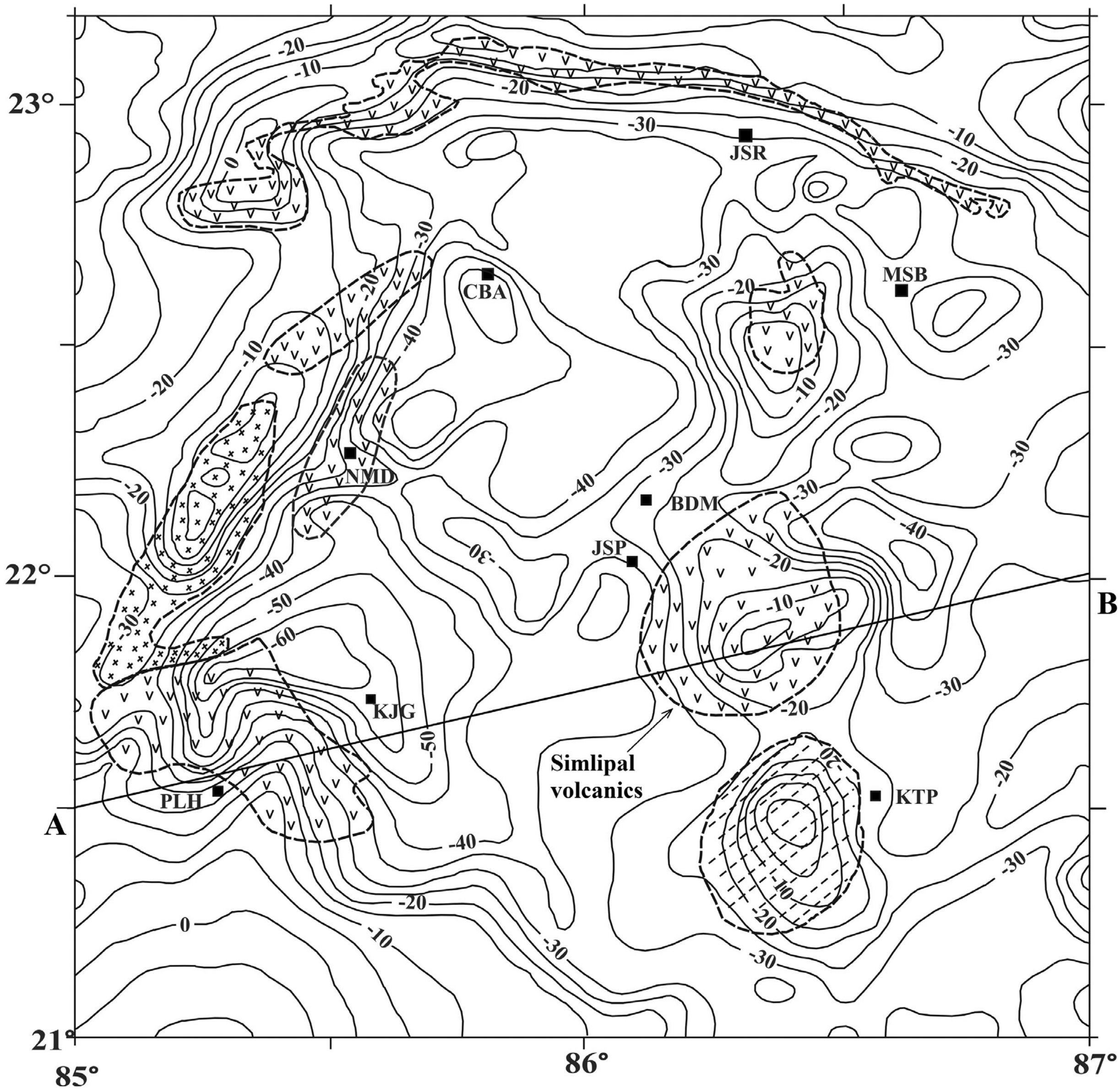

Fig. 18. Bouguer anomaly map (in mGal) of Sighbhum craton (Modified after Verma et al. (1984). JSR: Jamshedpur; MSB: Moosabani; CBA: Chaibasa; NMD: Noamundi; BDM: Badampahar; KTP: Kaptipada; KJG: Keonjhargarh; PLH: Pallalahara. v: volcanics; x: Iron Ore Group lavas and ultramafics. Slanted dashed lines: Proterozoic gabbro-anorthosite suites. AB is the location of the profile along which of the gravity model is presented (Fig. 19).

mantle plume near crust-mantle layer. Rare Earth Elements (REE) and HFSE patterns indicate their genesis within the spinel lherzolite field due to a relatively low degree of partial melting. They show enriched geochemical signatures, which can be attributed to the mixing of depleted asthenosphere melt with OIB type melt. The estimated mantle potential temperature (1300–1700 °C) and pressure (0.5–3.5 GPa) of these rocks, together with high elevation, positive gravity anomalies, thin lithosphere and thick magma underplating to the tune of 14 km indicate their mantle plume affinity. Subduction related geochemical signatures, as reported in a few earlier studies, have not been found.

Credit author statement

S.K. Dwivedi: Geochemical data analysis and writing of the manuscript
O.P. Pandey: Sample collection in the field and geophysical data analysis
Priyanka Tripathi: Petrography and geochemical data analysis
S.H. Jafri: Sample collection in the field and petrography
D. Srinivasa Sarma: SEM studies
A Narsing Rao: Review and editing
Prachiti Kanakdande: Geochemical data analysis
G. Parthasarathy: Review and editing

Declaration of competing interest

The authors declare no potential conflict of interest

Acknowledgements

We are extremely thankful to Dr. A. Vasanthi, the handling Editor and the reviewers for their constructive comments and helpful suggestions which have improved the manuscript enormously. We are also thankful to the Drs. S. Nirmal Charan and D.V. Subbarao for helpful discussions. Drs. V. Balram, M. Satyanarayanan and A.

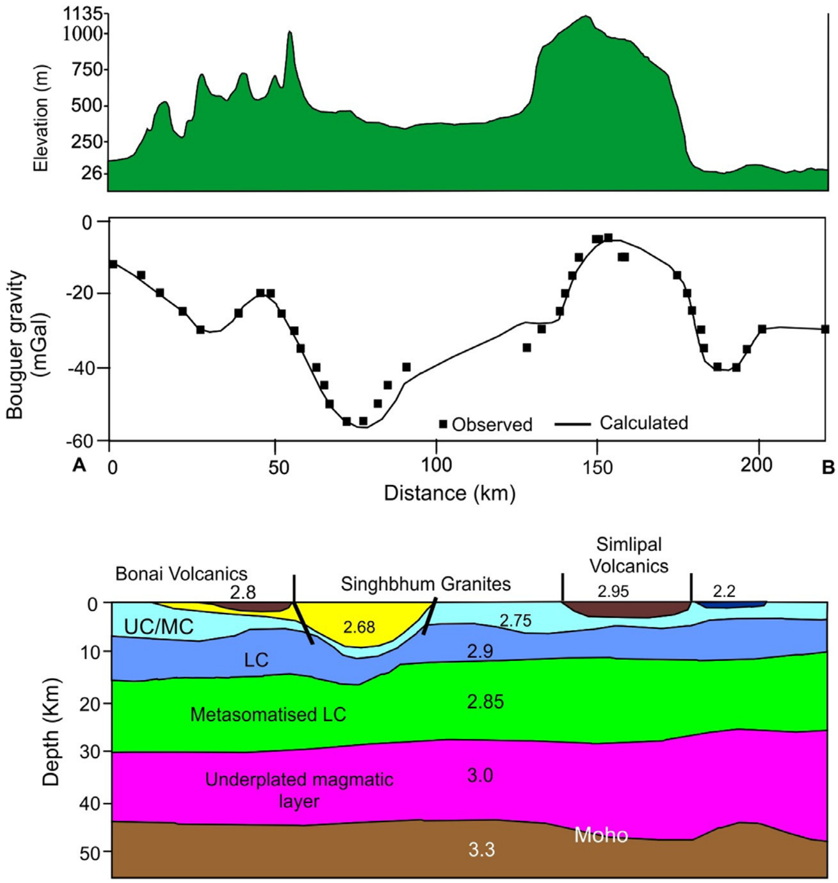

Fig. 19. $2^{1/2}$ gravity model and inferred crustal density variation along the profile AB (location is shown in Fig. 18). Elevation variation along the profile is also given.

Keshav Krishna have provided help in the acquisition of geochemical data by ICPMS and XRF. G. Parthasarathy is grateful to NIAS and INSA for the support under the INSA Senior Scientist scheme. O.P. Pandey thanks CSIR (New Delhi) for granting Emeritus Scientist position at CSIR-National Geophysical Research Institute, Hyderabad. The permission accorded by the Director, CSIR-National Geophysical Research Institute Hyderabad to publish this work is gratefully acknowledged.

References

Acharyya, S.K., 1993. Greenstones from Singhbhum Craton, their Archaean character, oceanic crustal affinity and tectonics. Proc. National Acad. Sci. (Earth Planet. Sci.) India 64 (A), 211–222.
Acharyya, S.K., Gupta, A., Orihasi, Y., 2010a. New U-Pb zircon ages from Paleo-Mesoarchean TTG gneisses of the Singhbhum craton, eastern India. Geochem. J. 44, 81–88.
Acharyya, S.K., Gupta, A., Orihasi, Y., 2010b. Neoarchean-Paleoproterozoic stratigraphy of the Dhanjori basin, Singhbhum craton, eastern India: and recording of a few U-Pb zircon dates from its basal part. J. Asian Earth Sci. 39, 527–536.
Aldanmaz, E., 2002. Mantle source characteristics of alkali basalts and basanites in an extensionalintracontinental plate setting, western Anatolia, Turkey: implications for multi-stage melting. Int. Geol. Rev. 44, 440–457.
Alvi, S.H., Raza, M., 1991. Nature and magma type of Jagannathpurvolcanics, Singhbhum, Eastern India. J. Geol. Soc. India 38, 524–531.
Alvi, S.H., Raza, M., 1992. Geochemical evidence for the volcanic arc tectonic setting of DhanjoriVolcanics, Singhbhum Craton, Eastern India. Geol. Mag. 29, 337–348.
Kumar, Anil, Parasuramulu, V., Shankar, Ravi, Besse, J., 2017. Evidence of a Neoarchean LIP in the Singhbhum craton, eastern India: implications to Vaalbara supercontinent. Precambrian Res 292, 163–174.
Arif, M., Dey, S., Gond, A.K., Zong, K., Liu, Y., Mitra, A., Sarangi, S., 2021. Mesoarchean continental intraplate volcanism and sedimentation: the case of the Simlipal basin, Singhbhum Craton, eastern India. Precambrian Res 361, 106245.
Arndt, N.T., Lesher, C.M., Barnes, S.J., 2008. Komatiite. Cambridge Univ. Press.
Artemieva, I.M., Mooney, W.D., 2001. Thermal thickness and evolution of Precambrian lithosphere: a global study. J. Geophys. Res. 106, 16387–16414.
Balaram, V., Rao, T.G., 2003. Rapid determination of REEs and other Trace Elements in Geological samples by Microwave Acid Digestion and ICP-MS. Atom. Spec. 24 (6), 206–212.
Bandyopadhyay, P.K., Chakrabartil, A.K., DeoMurari, M.P., Misra, S., 2001. 2.8 Ga Old Anorogenic Granite-Acid Volcanics Associationfrom Western Margin of the Singhbhum-Orissa Craton,Eastern India. Gond. Res. 4, 465–475.
Banerjee, P.K., 1982. Stratigraphy, petrology and geochemistry of some Precambrian basic volcanic and associated rocks of Singhbhum district, Bihar and Mayurbhanj and Keonjhar districts. Orissa. Mem. Geol. Surv. India 111, 54.
Banerjee, M., Ray, J., Adhikary, N., Nandy, S., Manikyamba, C., Pauli, M., Chakraborthy, D., Eslami, A., 2016. Experimental studies to constrain parental magma of Malangtoli volcanics from Singhbhum craton of the eastern Indian Shield. J. Geol.Soc. India 88, 245–255.
Basu, A., Maitra, M., Roy, P.K., 1997. Petrology of mafic-ultramafic complex of Sukinda Valley. Orissa. Indian Miner. 50, 271–290.
Bedard, J.H., 2006. Trace element partitioning in plagioclase feldspar. Geochim. Cosmochim. Acta 70, 3717–3742.
Bose, M.K., 2009. Precambrian mafic magmatism in the Singhbhum craton, eastern India. J. Geol. Soc. India 73, 13–35.
Cao, Q., van der Hilst, R.D., De Hoop, M.V., Shim, S.H., 2011. Seismic imaging of transition zone discontinuities suggests a hot mantle west of Hawaii. Science 332, 1068–1071.
Chapman, D.S., Pollack, H.N., 1977. Regional geotherms and lithospheric thickness. Geology 5, 265–268.
Chaudhuri, T., 2020. A review of Hadean to Neoarchean crust generation in the Singhbhum Craton, India and possible connection with Pilbara Craton, Australia: the geochronological perspective. Earth Sci. Rev. 202, 103085.
Chaudhuri, T., Wan, Y., Mazumder, R., Ma, M., Liu, D., 2018. Evidence of enriched, Hadean mantle reservoir from 4.2 to 4.0 Ga zircon xenocrysts from Paleoarchean TTGs of the Singhbhum craton. Eastern India. Scientific Reports 8, 7069. doi:10.1038/s41598-018-25494-6.
Christensen, N.I., Mooney, W.D., 1995. Seismic velocity structure and composition of the continental crust; a global view. J. Geophy. Res. 100, 9761–9788.
Condie, K.C., 2005. TTG and adakites: are they both slab melts? Lithos 80, 33–44.
Curray, J.R., Munasinghe, T., 1991. Origin of the Rajmahal Traps and the 87°E ridge: preliminary reconstructions of the trace of the crozet hotspot. Geology 19, 1237–1240.
Davies, G.F., 2009. Effect of plate bending on the Urey ratio and the thermal evolution of the mantle. Earth Planet. Sci. Lett. 287, 513–518.

Davies, J.F., Grant, R.W.E., Whitehead, R.E.S., 1979. Immobile trace elements and Archaean volcanic stratigraphy in the Timmins mining area. Ontario. Can. J. Earth. Sci. 16, 305–311.
Davidson, J., Turner, S., Plank, T., 2013. Dy/Dy*: variations arising from mantle sources and petrogenetic processes. J. Petro. 54, 525–537.
Desharnais, G., 2005. Geochemical and Isotopic Investigation of Magmatism in the Fox River Belt: Tectonic and Economic Implications 207 PhD thesis.
Dey, S., Moyen, J., 2020. Archean granitoids of India: windows into early Earth tectonics. Geol. Soc. London 489 https://doi.org/10.1144/SP489-2020-155.
Dey, S., Topno, A., Liu, Y., Zong, K., 2017. Generation and evolution of Palaeoarchaean continental crust in the central part of the Singhbhum craton, eastern India. Precambrian Res 98, 268–291.
Dey, S., Mitra, A., Nandy, J., Mondal, S., Topno, A., Liu, Y., Zong, K., 2019. Early Crustal Evolution As Recorded in the Granitoids of the Singhbhum and Western Dharwar Cratons. Earth's Oldest Rocks. Elsevier doi:10.1016/B978-0-444-63901-1.00030-7.
Dong, Y., Xiao, L., Zhou, H., Du, J., Zhang, N., Xiang, H., Wang, C., Zhao, Z., Huang, H., 2010. Volcanism of the Nanpu Sag in the Bohai Bay Basin, Eastern China: geochemistry, petrogenesis, and implications for tectonic setting. J. Asian Earth Sci. 39, 173–191.
Farmer, G.L., 2014. Continental basaltic rocks. In: Rudnick, R.L. (Ed.), Treatise On Geochemistry. Elsevier, pp. 75–110. doi:10.1016/B978-0-08-095975-7.00303-X.
Frey, F.A., Dickey, J.S., Thompson, G., Bryan, W.B., Davis, H.L., 1980. Evidence for heterogeneous primary MORB and mantle sources. N.W. Indian Ocean. Contrib. Mineral. Petrol. 74, 387–402.
Geosoft Oasis Montaj, 2004. GM-SYS Version 7.0 Gravity and Magnetic Modeling Software User Guide. Northwest Geophysical Associates, Inc.
Ghosh, R., Vermeesch, P., Gain, D., Mondal, R., 2019. Genetic relationship among komatiites and associated basalts in the Badampahar greenstone belt (3.25-3.10 Ga), Singhbhum Craton, Eastern India. Precambrian Res 327, 196–211.
Greenough, J.D., Hayatasu, A., Papezik, V.S., 1998. Mineralogy, petrology and geochemistry of the alkaline Malpeque Bay sill, Prince Edward Island. Can Mineral 26, 97–108.
GSI-NGRI, 2006. Gravity Map Series of India on Scale 1:2000,000. Produced by Geological Survey of India, and CSIR-. National Geophysical Research Institute, Hyderabad, India.
Herzberg, C., Asimow, P.D., 2008. Petrology of some oceanic island basalts: PRIMELT2. XLS software for primary magma calculation. Geochem. Geophys. Geosyst. 9, 09001 Q.
Herzberg, C., Asimow, P.D., 2015. PRIMELT3 MEGA.XLSM software for primary magma calculation: peridotite primary magma MgO contents from the liquidus to the solidus. Geochem. Geophys. Geosyst. 16 (2), 563–578.
He, Q., Xiao, L., Balta, B., Gao, R., Chen, J., 2010. Variety and complexity of the Late Permian Emeishan basalts: reappraisal of plume-lithosphere interaction processes. Lithos 119, 91–107.
Hofmann, A., Mazumder, R., 2015. A review of the current status of the Older Metamorphic Group and Older Metamorphic Tonalite Gneiss: insights into the Palaeoarchaean history of the Singhbhum craton, India. Geological Society, London, Memoirs 43 (1), 103–107.
Huppert, H.E., Sparks, R.S.J., 1985. Komatiites I: eruption and flow. J. Petrology 263, 694–725.
Irvine, T.N., Baragar, W.R.A., 1971. A guide to the chemical classification of the common volcanic rocks. Can. J. Earth Sci. 8, 523–548.
Ishikawa, Y., Sawaguchi, T., Iwaya, S., Horiuchi, M., 1976. Delineation of prospecting targets for Kuroko deposits based on modes of volcanism of underlying dacite and alteration halos: mining. Geology 26, 105–117 (in Japanese with English abstract).
Jafri, S.S.H., Dwivedi, S.K., Pandey, O.P., Tripathi, P., Sarma, D.S., Krishna, A.K., Ramesh, S.L., Vidyasagar, G., 2021. Possible occurrence of Palaeoarcheanferropicrite cumulates and ferrobasalts in the Jojohatu area of North Singhbhum Craton, eastern India: evidence for a mantle plume source. Geol. J. 56, 5839–5862.
Jensen, L.S., 1976. A new cation plot for classifying subalkalic volcanic rocks. Ontario Division of Mines, Miscellaneous Paper 66, 22.
Katz, R.F., Spiegelman, M., Langmuir, C.H., 2003. A new parameterization of hydrous mantle melting. Geochem. Geophys. Geosyst. 4, 1073. doi:10.1029/2002GC000433.
Kinzler, R.J., 1997. Melting of mantle peridotite at pressures approaching the spinel to garnet transition: application to mid-ocean ridge basalt petrogenesis. J. Geophys. Res. 102, 853–874.
Korenaga, J., 2008. Urey ratio and the structure and evolution of Earth's mantle. Rev. Geophys. 46 (2). doi:10.1029/2007RG000241, http://dx.doi.org/.
Krishna, A.K., Murthy, N.N., Govil, P.K., 2007. Multielement analysis of soils by Wavelength-Dispersive X-ray Fluorescence Spectrometry. Atomic Spec 28, 202–214.
Kumar, P., Ravi Kumar, M., Srijayanthi, G., Arora, K., Srinagesh, D., Chadha, R.K., Sen, M.K., 2013. Imaging the lithosphere-asthenosphere boundary of the Indian plate using converted wave techniques. J. Geophys. Res., Solid Earth 118, 1–13. doi:10.1002/jgrb.50366.
Kuno, H., 1964. Igneous Rock series: Chemistry of the Earth's crust 2 109–121 (in Russian).
Kurkcuoglu, B., 2010. Geochemistry and petrogenesis of basaltic rocks from the Develidag volcanic complex, Central Anatolia, Turkey. J. Asian Earth Sci., 37, 42–51.
Kushiro, I., 1996. Earth Processes: Reading the Isotopic Code 109, 122 95 (eds Basu, A. & Hart, S.).
Lai, S., Qin, J., Li, Y., Li, S., Santosh, M., 2012. Permian high Ti/Y basalts from the eastern part of the Emeishan Large Igneous Province, southwestern China: petrogenesis and tectonic implications. J. Asian Earth Sci. 47, 216–230.
Large, R.R., Gemmell, J.B., Paulick, H., Huston, D.L., 2001. The alteration box plot: asimpleapproach to understanding the relationship between alteration mineralogy andlithogeochemistry associated with volcanic-hosted massive sulfide deposits. Econ.Geol 96, 957–971.
Lassiter, J.C., DePaolo, D.J., 1997. Plume/lithosphere interaction in the generation of continental and oceanic flood basalts: chemical and isotopic constraints. Geophys. Monogr.-Am. Geophys. Union 100, 335–356.
Le Bas, M.J., Le Maitre, R.W., Streckeisen, A., Zanettin, B., 1986. A chemical classification of volcanic rocks based on the total alkali-silica diagram. J. Petrol. 27, 745–750.
Lee, C.-T.A., Luffi, P., Plank, T., Dalton, H., Leeman, W.P., 2009. Constraints on the depths and temperatures of basaltic magma generation on Earth and other terrestrial planets using new thermobarometers for mafic magmas. Earth Planet. Sci. Lett. 279, 20–33.
Li, S.R., Santosh, M., 2014. Metallogeny and craton destruction: records from the North China Craton. Ore Geol. Rev. 56, 376–414.
Mahadevan, T.M., 2002. Geology of Bihar and Jharkhand: Geol. Soc. India, Bangalore, 563pp.
Mandal, P., 2017. Lithospheric thinning in the eastern Indian craton: evidences for lithospheric delamination below the Archean Singhbhum craton. Tectonophysics 608, 91–108.
Manikyamba, C., Ray, J.S., Ganguli, S., Singh, M.R., Santosh, M., Saha, A., Satyanaraynan, M., 2015. Boniniticmetavolcanic rocks and island arc tholeiites from the older metamorphic group (OMG) of Singhbhum craton, eastern India: geochemical evidence for Archean subduction process. Precambrian Res 271, 138–159.
Manikyamba, C., Ganguly, S., Santosh, M., Subramanyam, K.S.V., 2017. Volcano-sedimentary and metallogenic records of the Dharwar greenstone terranes, India: window to Archean plate tectonics, continent growth, and mineral endowment. Gond. Res. 50, 38–66.
Manikyamba, C., Pahari, A., Santosh, M., Ray, J., Sindhuja, C.S., Subramanyam, K.S.V., Singh, M.R., 2020. Mesoarchean gabbro-anorthosite complex from Singhbhum Craton, India. Lithos 366-367, 105541.
Mazumder, R., De, S., Ohta, T., Flannery, D., Mallik, L., Chaudhury, T., Chatterjee, P., Ranaivoson, M.A., Arima, M., 2015. Paleo-Mesoproterozoic sedimentation and tectonics of the Singhbhum Craton, eastern India, and implications for global and craton-specific geological events. Geol. Soc. London Mem. 43 (1), 139–149. doi:10.1144/M43.10.
Menzies, M.A., Kyle, P.R., Jones, M., Ingram, G., 1991. Enriched and depleted source components for tholeiitic and alkaline lavas from Zuni-Bandera, New Mexico: inferences about intraplate processes and stratified lithosphere. J. Geophys. Res. 96, 13645–13671.
Middlemost, E.A., 1989. Iron Oxidation Ratios, Norms and the Classification of Volcanic Rocks. Chem. Geol. 77, 19–26. doi:10.1016/0009-2541(89)90011-9.
Misra, S., 2006. Precambrian chronostratigraphic growth of Singhbhum-Orissa craton, eastern Indian Shield: an alternative model. J. Geol. Soc. India 67, 356–378.
Misra, S., Johnson, P.T., 2005. Geochronological constraints on the evolution of the Singhbhum mobile belt and associated basic volcanics of eastern Indian Shield. Gond. Res. 8, 129–142.
Misra, S., Deomuari, M.P., Wiedenbeck, M., Goswami, J.N., Ray, S., Saha, A.K., 1999. $^{207}{}_{Pb}/^{206}{}_{Pb}$ Zircon ages and the evolution of the Singhbhum Craton, eastern India: an ion microprobe study. Precambrian Res 93, 139–151.
Mondal, S.K., Ribley, E.M., Robert Frei, C.L., 2006. The genesis of Archean chromite's fromNausahi and Sukinda massifs in the Singhbhum craton. India. Precambrian Res. 148, 45–66.
Mukhopadhyay, D., 2001. The Archaean nucleus of Singhbhum: the present state of knowledge. Gond. Res. 4, 307–318.
Mukhopadhyay, D., Dutta, D.R.Sinha-Roy, S. (Ed.), 1983. Structures in the Roro ultramafics and their country rocks, Singhbhum district, Bihar. (Ed) Structure and Tectonics of Precambrian Rocks of India: Recent Researches in Geology 98–109 10.
Mukhopadhyay, D., Matin, A., 2020. The Architecture and Evolution of the Singhbhum Craton. Episodes 43, 19–50.
Mukhopadhyay, J., Ghosh, G., Zimmermann, U., Guha, S., Mukherjee, T., 2012. A 3.51 Ga bimodal volcanic-BIF-ultramafic succession from Singhbhum Craton: implications for Palaeoarchaean geodynamic processes from the oldest greenstone succession of the Indian subcontinent. Geol. J. l47, 284–311.
Negi, J.G., Pandey, O.P., Agrawal, P.K., 1986. Super mobility of hot Indian lithosphere. Tectonophysics 131, 147–156.
Negi, J.G., Agrawal, P.K., Pandey, O.P., 1987. Large variation of Curie-depth and lithospheric thickness in Indian sub-continent and a case for magneto-thermometry. Geophys. J. R. Astron. Soc. 88, 763–775.
Nelson, D.R., Bhattacharya, H.N., Thern, E.R., Altermann, W., 2014. Geochemical and ion- microprobe U-Pb zircon constraints on the Archean evolution of Singhbhum Craton, eastern India. Precambrian Res 255, 412–432.
Olierook, H.K.H., Clarka, C., Reddya, S.M., Mazumder, R., Jourdana, F., Evansa, N.J., 2019. Evolution of the Singhbhum Craton and supracrustal provinces from age, isotopic and chemical constraints. Earth. Sci. Rev. 193, 237–259.
Pahari, A., Tang, L., Manikyamba, C., Santosh, M., Subramanyam, K.S.V., Ganguly, S., 2019. Meso-Neoarchean magmatism and episodic crustal growth in the Kudremukh-Agumbe granite-greenstone belt, western Dharwar Craton, India. Precambrian Res 323, 16–54.
Pandey, O.P., 2016. Deep scientific drilling results from Koyna and Killari earthquakeregions reveal why Indian shield lithosphere is unusual, thin and warm. Geosci. Front. 7, 851–858.

Pandey, O.P., 2020. Geodynamic Evolution of the Indian Shield: Geophysical aspects. Springer International Publishing, p. 349. doi:10.1007/978-3-030-40597-7.
Pandey, O.P., Agrawal, P.K., 1999. Lithospheric mantle deformation beneath the Indian cratons. J. Geology 107, 683–692.
Pandey, O.P., Vedanti, N., Srivastava, R.P., Uma, V., 2013. Was Archean Dharwar craton ever stable? Aseismic perspective. J Geol. Soc. India 81, 774–780.
Pandey, O.P., Tripathi, P., Parthasarathy, G., Rajagopalan, V., Sreedhar, B., 2014. Geochemical and mineralogical studies of chlorine-rich amphibole and biotite from the 2.5 Ga mid-crustal basement beneath the 1993 Killari earthquake region, Maharashtra, India: evidence for mantle metasomatism beneath the Deccan traps? J. Geol. Soc. India 83, 599–612.
Pandey, O.P., Tripathi, P., Vedanti, N., Sarma, S.D., 2016. Anomalous seismic velocity dropin iron and biotite rich amphibolite to granulite facies transitional rocks from Deccan volcaniccovered 1993 Killari earthquake region, Maharashtra (India): a case study. Pure Appl. Geophys. 173, 2455–2471.
Pandey, O.P., Mezgera, K., Ranjan, S., Upadhyay, D., Villaa, I.M., Naglera, T.F., Vollstaedta, H., 2019. Genesis of the Singhbhum Craton, eastern India; implications for Archean crust-mantle evolution of the Earth. Chem. Geol. 512, 85–106.
Pearce, J.A., 1996. A user's guide to basalt discrimination diagrams. In: Wyman, DA (Ed.), Trace Element Geochemistry of Volcanic Rocks: Applications for Massive Sulphide Exploration. Geol. Assoc. Can., pp. 79–113 12.
Pearce, J.A., 2008. Geochemical fingerprinting of oceanic basalts with applications toophiolite classification and the search for Archean oceanic crust. Lithos 100, 14–48.
Polat, J., Anderson, D.L., 1995. Depth extent of cratons as inferred from tomographic studies. Geology 23, 205–208.
Polat, A., Hofmann, A.W., 2003. Alteration and geochemical patterns in the 3.7-3.8 Ga Isua greenstone belt, West Greenland. Precambrian Res 126, 197–218.
Polat, A., Kerrich, R., Wyman, D.A., 1999. Geochemical diversity in oceanic komatiites and basalts from the late Archean Wawa greenstone belts, Superior Province, Canada: trace element and Nd isotope evidence for a heterogeneous mantle. Precambrian Res 94, 139–173.
Rajesh, H.M., Chisonga, B.C., Shindo, K., Beukes, N.J., Armstrong, R.A., 2013. Petrographic, geochemical and SHRIMP U-Pb titanite age characterization of the Thabazimbi mafic sills: extended time frame and a unifying petrogenetic model for the Bushveld Large Igneous Province. Precambrian Res 230, 79–102.
Ramakrishnan, M., Vaidyanadhan, R., 2008. Geology of India 994.
Rantsman, E.Ya., Chetty, T.R.K., Rao, M.N., Glasko, M.P., Zhidkov, M.P., Gorshkov, A.I., 1995. Explanatory Broacher. Map of Morphostructural Zoning of the Himalayan Belt Himalayan Fore Deep and the Indian Shield. D.S.T., New Delhi 29.
Rasheed, K., SrinivasaSarma, D., Asokan, A.D., Dash, J.K., Bhutani, R., 2021. A non-arc tectonic setting for the evolution of Archean gabbro anorthosite Complexes: evidence from the Singhbhum Craton, eastern India. Precambrian Res 363, 106250.
Shankar, Ravi, Sarma, S.D., Ramesh Babu, N., Parashuramulu, V., 2018. Paleomagnetic study of 1765 Ma dyke swarm from Singhbhum Craton: implications to the Paleogeography of India. J. Asian Earth Sci. 157, 235–244.
Ray, J., Das, S., Bhattacharyya, P., 2006. Malangtoli Lava of the Eastern Indian Shield: Some Aspects of Major-Element Geochemistry and Tectonic Affiliation 55–68 60.
Raza, M., Alvi, S.H., Abu-Hamatteh, Z.S.H., 1995. Geochemistry and Tectonic significance of Ongarbiravolcanics, Singhbhum Craton, Eastern India. J. Geol. Soc. India 45, 643–652.
Rogers, J.J.W., Callahan, E.J., 1987. Radioactivity, heat flow and rifting of the Indian continental crust. J. Geol. 95, 829–836.
Rollinson, H.R., 1993. Using Geochemical data: Evaluation, presentation, Interpretation Longman. Essex, p. 352.
Rollinson, H.R., 2014. Using geochemical data: evaluation, presentation, interpretation.
Roy, A.B., Bhattacharya, H.N., 2012. Tectonostratigraphic and Geochronologic Reappraisal Constraining the Growth and Evolution of Singhbhum Archaean Craton, Eastern India. J. Geol. Soc. India 80, 455–469.
Roy, A., Sarkar, A., Jayakumar, S., Aggrawal, S.K., Ebihara, M., Satoh, H., 2005. Late Archaean mantle metasomatism below eastern Indian craton: evidence from trace elements, REE geochemistry and Sr-Nd-O isotope systematics of ultramafic dykes. Proc. Indian Acad. Sci. (Earth and Planet. Sci.) 113, 649–665.
Rudnick, R.L., Gao, S., 2003. The composition of the continental crust. In: Rudnick, R.L., Holland, H.D., Turekian, K.K. (Eds.), Treatise on Geochemistry - The Crust. Elsevier, Oxford, pp. 1–64.
Saccani, E., 2015. A new method of discriminating different types of post-Archean ophiolitic basalts and their tectonic significance using Th-Nb and Ce-Dy-Yb systematic. Geosci. Front. 6, 481–501.
Saha, A.K., 1994. Crustal evolution of Singhbhum, North Orissa, eastern India. Mem. Geol. Soc. Ind. 27, 341.
Saha, L., Hofmann, A., Xie, H., 2012. Archaean evolution of the Singhbhum Craton: constraints from new metamorphic-geochemical data and SHRIMP zircon ages. In: Craton Formation and Destruction with Special Emphasis On BRICS Cratons. University of Johannesburg, South Africa, pp. 7–9.
Salters, V.J.M., Stracke, A., 2004. Composition of the depleted mantle. Geochem. Geophy. Geosy. 5 (5), Q05004. doi:10.1029/2003GC000597.
Sarkar, S.N., Ghosh, D., Lambert St, R.J., 1986. Rubidium-strontium and lead isotopicstudies on the Soda Granites from Mosaboni, Singhbhum copper belt, E. India. Indian J. Earth Sci. 13, 101–116.
Sarma, A.U.S., 1980. Study and Analysis of Gravity Field Over Singhbhum and Adjoining Area. Indian School of Mines, Dhanbad Ph.D. thesis.
Sengupta, S., Acharyya, S.K., deSmeth, J.B., 1997. Geochemistry of Archaean volcanic rocks from Iron Ore Supergroup, Singhbhum, Eastern India. Proc. Indian Acad. Sci. (Earth Planet. Sci.) 106, 327–342.
Shalivahan, Bhattacharya, B.B., Chalapathi Rao, N.V., Maurya, V.P., 2014. Thin lithosphere-asthenosphere boundary beneath Eastern Indian craton. Tectonophysics 612-613, 128–133.
Sharma, R.S., 2009. Cratons and Fold Belts of India. Springer, p. 304.
Simonov, V.A., Mikolaichuk, A.V., Safonova, I., Yu Kotlyarov, A.V., Kovyazin, S.V., 2014. Late Paleozoic-Cenozoic intra-plate continental basaltic magmatism of the Tienshan-Junggar region in the SW Central Asian Orogenic Belt. Gond. Res. 27, 1646–1666 https://doi.org/10.1016/j. gr.2014.03.001.
Singh, M.R., Manikyamba, C., Ganguli, S., Ray, J., Santosh, M., Singh, T.D., Kumar, B.C., 2017. Paleoproterozoic arc basalt-boninite-high magnesian andesite-Nb enriched basalt association from the Malangtoli volcanic suite, Singhbhum craton, eastern India: geochemical record for subduction initiation to arc maturation continuum. J. Asian Earth Sci. 134, 191–206.
Song, X.Y., Zhou, M.F., Keays, R.R., Cao, Z.M., Sun, M., Qi, L., 2006. Geochemistry of the Emeishan flood basalts at Yangliuping, Sichuan, SW China: implications for sulfide segregation. Contrib. Mineral. Petrol. 152, 53–74.
Song, X.Y., Qi, H.W., Robinson, P.T., Zhou, M.F., Cao, Z.M., Chen, L.M., 2008. Melting of the subcontinental lithospheric mantle by the Emeishan mantle plume: evidence from the basal alkaline basalts in Dongchuan, Yunan, Southwestern China. Lithos 100, 93–111.
Sreenivas, B., Dey, S., Bhaskar Rao, Y.J., Vijaya Kumar, T., Babu, E.V.S.S.K., William, I.S., 2019. A new cache of Eoarchean detrital zircons from Sighbhum craton, eastern India and constraints on early Earth geodynamics. Geosci. Front. 10, 1359–1370.
Sun, S.S., McDonough, W.F., 1989. Chemical and isotopic systematic of oceanic basalts: implications for mantle composition and process. In: Saunders, A.D., Norrey, M.J. (Eds.), Magmatism in the Ocean Basins. Geol. Soc. London. Spl. Publ., pp. 313–345 42.
Taylor, S.R., McLennan, S.M., 1985. The Continental Crust: Its Composition and Evolution. Black well Scientific Publications, Oxford, p. 312.
Teng, X., Santosh, M., 2015. A long-lived magma chamber in the Paleoproterozoic North China Craton. Evidence from the Damiao gabbro-anorthosite suites. Precambrian Res 256, 79–101.
Thornton, C.P., Tuttle, O.F., 1960. Chemistry of igneous rocks: pt. 1. Differentiation index. American J. Science 258, 664–684.
Tiwari, V.M., Ravi Kumar, M., Mishra, D.C., 2013. Long wavelength gravity anomalies over India: crustal and lithospheric structures and its flexure. J Asian Earth. Sci. 70-71, 169–178.
Tripathi, P., Parthasarthy, G., Massood Ahmad, S.M., Pandey, O.P., 2012. Mantle- derived fluids in the basement of the Deccan trap: evidence from stable carbon and oxygen isotopes of carbonates from the Killari borehole basement, Maharastra, India. Int. J. Earth. Sci. 101, 1385–1395.
Upadhyay, D., Chattopadhyay, S., Kooijman, E., Mezger, K., Berndt, J., 2014. Magmatic and metamorphic history of Paleoarchean tonalite-trondhjemite-granodiorite (TTG) suite from the Singhbhum craton, eastern India. Precambrian Res 252, 180–190. doi:10.1016/j.precamres.2014.07.011.
Upadhyay, D., Chattopadhyay, S., Mezger, K., 2019. Formation of Paleoarchean-Mesoarchean Na-rich (TTG) and K-rich granitoid crust of the Singhbhum craton, eastern India: constraints from major and trace element geochemistry and Sr-Nd-Hf isotope composition. Precambrian Res 327, 255–272.
Van Hunen, J., Moyen, J.F., 2012. Archean Subduction: fact or Fiction? Annu. Rev. Earth Planet. Sci. 40 (1), 195–219. doi:10.1146/annurev-earth-042711-105255.
Vasanthi, A., Santosh, M., 2021. Overview of regional gravity field computation models and application of a novel method in imaging the lithospheric architecture and destruction of the North China Craton. Earth Sci. Rev. 215, 103548.
Vasanthi, A., Singh, A.P., Kumar, N., Nageswara Rao, B., Satyakumar, A.V., Santosh, M., 2021. Crust-mantle structure and lithospheric destruction of the oldest craton in the Indian Shield. Precambrian Res 362, 106280.
Verma, R.K., Mukhopadhyay, M., Roy, S.K., Sinha, R.P.P., 1978. An analysis of gravity field over North Singhbhum. Tectonophysics 44, 41–63.
Verma, R.K., Sarma, A.U.S., Mukhopadhyay, M., 1984. Gravity field over Singhbhum, its relationship to geology and tectonic history. Tectonophysics 106, 87–107.
Verma, S.P., Torres-Alvarado, I.S., Sotelo-Rodriguez, Z.T., 2002. SINCLAS: standard igneous norm and volcanic rock classification system. Comput. Geosci. 28, 711–715.
Verma, S.P., Torres-Alvarado, I.S., Velasco-Tapia, F., 2003. A revised CIPW norm. Schweiz Mineral Petrogr. Mitt. 83 (2), 197–216.
Walter, M.J., 1998. Melting of garnet peridotite and the origin of komatiite and depleted lithosphere. J. Petrol. 39, 29–60.
Wang, C., Song, S., Wei, C., Su, L., Allen, M.B., Niu, Y., Li, X., Dong, J., 2019. Palaeoarchaean deep mantle heterogeneity recorded by enriched plume remnants. Nat Geosci 12, 672–678.
Wolfe, C.J., Bjarnason, I.T., Van Decar, J.C., Solomon, S.C., 1997. Seismic structure of the Iceland mantle plume. Nature 385, 245–247.
Wu, W., Yang, J., Xu, Y., Wilde, S.A., Walker, R.J., 2019. Destruction of the North China Craton in the Mesozoic. Annu. Rev. Earth Planet. Sci. 47, 173–195.
Xia, Y., Xu, X., Zhao, G., Liu, L., 2015. Neoproterozoic active continental margin of the Cathaysia block: evidence from geochronology, geochemistry, and Nd-Hf isotopes of igneous complexes. Precambrian Res. 269, 195–216.
Xia, H., Thybo, H., Artemieva, M., 2017. Seismic crustal structure of the North China Craton and surrounding area: synthesis and analysis. J. Geophys. Res. Solid Earth 122, 5181–5207.

Xu, Y.G., Ma, J.L., Frey, F.A., Feigenson, M.D., Liu, J.F., 2005. Role of lithosphere–asthenosphere interaction in the genesis of Quaternary alkali and tholeiitic basalts from Datong, western North China Craton. Chem. Geol. 224, 247–271.
Zeng, X.W., Wang, M., Fan, J.J., Li, C., Xie, C.M., Liu, Y.M., Zhang, T.Y., 2018. Geochemistry and geochronology of gabbros from the Asa Ophiolite, Tibet: implications for the early cretaceous evolution of the Meso-Tethys Ocean. Lithos 320, 192–206.
Zhao, J.J., Zhou, M.F., 2007. Geochemistry of Neoproterozoic mafic intrusions in the Panzhihua district (Sichuan Province, SW China): implications for subduction related metasomatism in the upper mantle. Precambrian Res 152, 27–47.